



DIPLOMARBEIT

---

# Characterization of Vibrating Microstructures

ausgeführt zum Zwecke der Erlangung des akademischen Grades  
eines Diploms der technischen Wissenschaften unter der Leitung von

*Ao. Univ.-Prof. Dr. Franz Keplinger*  
Institut für Sensor- und Aktuatorssysteme

eingereicht an der Technischen Universität Wien  
Fakultät für Elektrotechnik und Informationstechnik

von

**Johan Wallin**

Lerchenfelderstrasse 50  
1080 Wien

Matr.-Nr. 0627983

Wien, im Juni 2015



# Contents

<b>1</b>	<b>Kurzfassung</b>	<b>iii</b>
<b>2</b>	<b>Abstract</b>	<b>v</b>
<b>3</b>	<b>Introduction</b>	<b>1</b>
3.1	Problem description . . . . .	1
3.2	History of the vibration sensor . . . . .	1
3.2.1	Piezoresistive accelerometer . . . . .	2
3.2.2	Capacitive accelerometer . . . . .	4
<b>4</b>	<b>Theory</b>	<b>7</b>
4.1	Harmonic oscillation . . . . .	7
4.2	Free damped oscillations . . . . .	9
4.3	Forced damped oscillations . . . . .	12
4.3.1	Oscillations with harmonic excitation of the mass . . . . .	13
4.3.2	Harmonic excitation of the foot point of the spring or of the damper	17
<b>5</b>	<b>Vibration Sensor</b>	<b>21</b>
5.1	Sensor design . . . . .	21
5.1.1	Mass . . . . .	22
5.1.2	Spring . . . . .	22
5.1.3	Capacitance . . . . .	23
<b>6</b>	<b>Production of Test Sensor</b>	<b>27</b>
6.1	Preparation . . . . .	27

6.2	Coating layer removal . . . . .	27
6.2.1	Coating layer removal . . . . .	28
6.2.2	Removal of SiO <sub>2</sub> to form ohmic conducts . . . . .	29
6.3	Structuring the metal layer . . . . .	29
6.4	Backside cavity . . . . .	32
<b>7</b>	<b>Micro System Analyzer</b>	<b>35</b>
7.1	Out-of-plane measuring mode . . . . .	36
7.2	In-plane measuring mode . . . . .	37
7.3	Topographical measuring mode . . . . .	39
7.4	Area of use for each mode . . . . .	40
7.5	Automation scripts . . . . .	41
7.5.1	In-plane automation script . . . . .	41
7.5.2	Out-of-plane automation script . . . . .	42
7.6	How to set up a measurement . . . . .	43
<b>8</b>	<b>Test environment</b>	<b>45</b>
8.1	Mechanical set-up . . . . .	45
8.2	Specifications of shaker . . . . .	45
8.3	Actuator input signal . . . . .	46
8.4	Piezoelectric actuator . . . . .	47
8.5	Spring . . . . .	49
8.6	Electrical estimations . . . . .	50
8.7	Assembly of shaker . . . . .	52

8.8	Evaluation of the test environment . . . . .	52
8.8.1	Harmonic motion . . . . .	53
8.8.2	Out-of-plane measurement set-up . . . . .	53
8.8.3	The shakers frequency dependence . . . . .	55
8.8.4	Voltage dependence . . . . .	59
8.9	Possible improvements of the shaker . . . . .	62
<b>9</b>	<b>Work flow for vibration sensor characterization</b>	<b>65</b>
<b>10</b>	<b>Results</b>	<b>67</b>
10.1	Optical evaluation . . . . .	67
10.2	Frequency dependence . . . . .	70
10.3	Correlation of analytical and measured frequency dependence . . . . .	74
	<b>Bibliography</b>	<b>75</b>
	<b>List of Figures</b>	<b>76</b>



# 1 Kurzfassung

Diese Arbeit stellt die Charakterisierung eines leichtgewichtigen Vibrationssensors dar. Thematisiert werden sowohl das Design des Sensors, als auch dessen Produktion. Hergestellt wurde der on-chip Vibrationssensor aus einem SOI (Silicon-on-Insulator) Wafer. Hierbei fand die MEMS (Micro-Electro-Mechanical-Systems) Technologie Anwendung. Um die Charakterisierung des Vibrationssensors zu ermöglichen, wurde eine Testumgebung geschaffen, die dabei ebenfalls analysiert sowie deren Daten dokumentiert wurden. Die durchgeführten Messungen wurden mit Hilfe eines MSA (Micro System Analyzer) ermittelt. Dieses Messgerät ermöglicht es, genaue Messungen von in-plane und out-of-plane Bewegungen zu erheben.



## 2 Abstract

This thesis presents the characterization of a lightweight vibration sensor. The design of the sensor as well as the production procedure will be handled. The on-chip vibration sensor is fabricated out of a SOI (Silicon-on-Insulator) wafer using MEMS (micro-electro-mechanical-systems) technologies. Additionally a vibrating test environment is built and characterized to evaluate the sensor. The characterization measurements are performed by a MSA (Micro System Analyzer) which can accurately detect in-plane and out-of-plane movements.



## **3 Introduction**

### **3.1 Problem description**

A micromachined sensor system consists of a mechanical structure, with a feature size down to a few micrometers and overall dimensions size of up to a few millimeters [1], along with electrical contacts for the mechanical measurand. When mechanical systems are scaled down to the micrometer level, quantities that have little or no effect in the macroscopic world suddenly become dominating factors [2]. Typical phenomena are sticking, air damping or electrostatic effects.

This thesis includes the manufacturing of a vibration sensor. The different production steps will be presented, together with an optical analysis of the produced prototypes. On each wafer there is a set of different sensors. The individual versions will resonate at a certain frequency, which is ascertained by a well defined design. The thesis presents correspondence of calculated and measured resonance frequencies and the frequency dependence within the operating frequency span.

In order to evaluate the sensor's frequency response, a test environment was developed. It excites vibrations for the sensor by using a piezoelectric based actuator. Since these vibrations act as reference signal, the actuator system itself will also be characterized in respect to frequency and voltage dependence.

The electrical output of the sensor is generated by a capacitive readout. However, this aspect will not be handled in this thesis but rather the mechanical properties.

### **3.2 History of the vibration sensor**

In the 1960's the development of silicon technology increased rapidly [3]. The excellent mechanical, electrical and thermal properties were described and initial research was done to apply silicon as a mechanical material. It was also found that silicon could act as a piezoresistive material. At that time, the dominating method used for mechanical sensors was to measure resistance change through strain. One of the advantages with piezoresistive sensing that was found was the anisotropic behavior of the material which

is beneficial by directional sensing. Also, the piezoresistive effect was much higher, up to two magnitudes larger, than for metal strain gauges. These properties give silicon the fundamental possibility of being a mechanical as well as a sensing material. Additionally, a mechanical structure together with sensors and electronics can be built in the same material on one chip.

The first sensor developed in this technology was presented in 1962 [4]. It was a pressure sensor consisting of a silicon diaphragm with piezoresistors on top. This early model was not a fully silicon micromachined sensor in the sense that it was not constructed directly out of a silicon wafer but the diaphragm plate was bonded onto a metal frame. The design principle for pressure sensors, however, is still widely used today.

### **3.2.1 Piezoresistive accelerometer**

Through the accomplishment of mass production micromachined pressure transducer, research was concentrated toward development of a silicon piezoresistive micromachined accelerometer. The mechanical structure of an accelerometer is more complex than that of a pressure transducer which stalled the development and the first prototype was presented 1979 [5] (see Figure 3.1), 17 years after the first pressure transducer.

The mass is connected to the static frame by a thin beam. Two piezoresistors are formed, one on the frame and one on the beam to create a half bridge. When the structure is accelerated perpendicular to the frame plane, the mass causes the beam to be bent. This results in an electrical resistance change and, therefore, also a voltage change in the half bridge, directly proportional to the acceleration.

Still today, the basic design principle of the piezoresistive accelerometer remains the same. There were, however, a few complications to get the accelerometer prototype into mass production. The prototype suffered from two main problems. Firstly, it was optimized for high sensitivity by choosing a thin and narrow beam together with a large mass. Say that the sensor was designed for a working range of a few g. A shock of theoretically 100 times larger, produced by dropping the device/sensor, would cause a large risk of breaking the thin beam. An overload displacement protection of the system was consequently needed.

The second issue concerned the damping of the system. The frequency response for

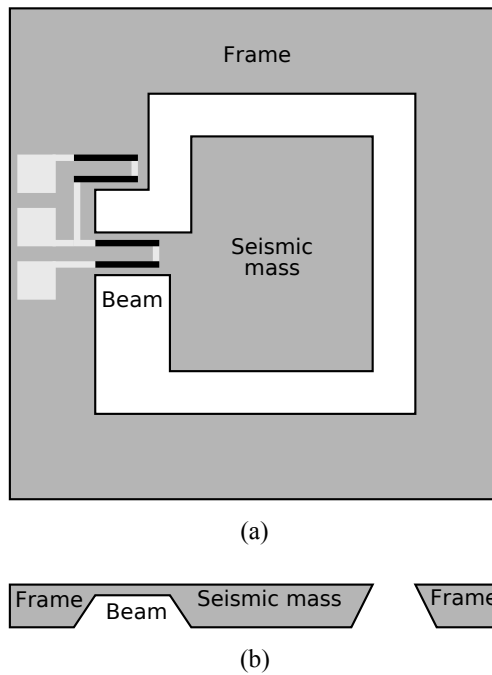


Figure 3.1: Schematic of the very first cantilever structure prototype for acceleration sensing: (a) top view, (b) cross section view.

this prototype device had a high  $Q$ -value, i. e., the sensor strongly resonates at a certain frequency. This reduces the bandwidth as well as once again introduces the risk of breaking the beam due to a large displacement at the resonance frequency. One solution that solved both issues was presented in the 1980s. The sensor plate was encapsulated in between two plates, with a thin air layer on top and bottom face of the plate (see Figure 3.2). The thin film of air provides additional damping for the system. The damping ratio can be controlled by choosing the air film thickness. Also, the overload problem was solved by adding a bumper to each encapsulating plate.

Since the damping and overload issue was solved with this design piezoresistive accelerometers started to be mass produced in the late 1980s [6].

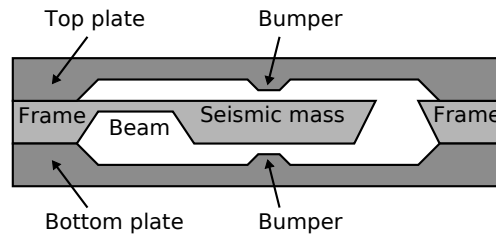


Figure 3.2: Schematic of the cross section of a bulk machined accelerometer with overload protection and air damping.

### 3.2.2 Capacitive accelerometer

The operation of piezoresistive sensing as well as production methods are well developed. The signal processing is also simple to process due to high linearity. The technology does, however, suffer from some drawbacks. Since the sensing is based on stress, the packaging of the device is critical. Any stress caused by packaging can cause a large offset. Also for applications where a very high accuracy is demanded, the temperature dependence of piezoelectric resistance causes a voltage offset, meaning that each individual sensor must be calibrated before every operation. Because of these properties a capacitive system was developed which depends more on stable mechanical properties of the sensor material than the piezoresistive properties.

The first prototype for a capacitive micromachined transducer was a pressure sensor. It used the same type of design principle as the piezoresistive version. Only instead of measuring the mechanical stress of the membrane the capacitive change between membrane and a glass plate was probed, on which the membrane was mounted. This type of sensor did not have any greater commercial success due to production complications and more importantly because of a nonlinear output.

The capacitive accelerometer was, however, well received on the market. They have been developed to feature high resolution together with low production cost by using the well developed surface micromachining technology. The initial development was based on the bulk micromachined piezoresistive version (see Figure 3.2). The modified capacitive version can be seen in Figure 3.3.

The seismic mass in this setup acts as one of three electrodes. When the sensor is not

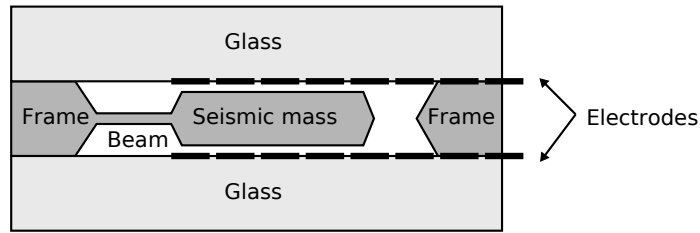


Figure 3.3: Schematic of the cross section of a bulk machined capacitive accelerometer.

exposed to any acceleration, the seismic mass is in a steady state. The capacitances on each side of the mass toward the electrodes are the same since the face area as well as the distance of the gaps are identical. When the sensor is accelerated the mass is displaced, changing the gap distance to each electrode and, consequently, the individual capacitances. One of the capacitances will be increased and the other one decreased.

Efforts were made to develop a capacitive accelerometer in the surface micromachined technology with the motivation of better accuracy and mass production properties compared to bulk micromachining. Figure 3.4 shows an example of such a structure. In this set up the mass can be displaced in an in-plane motion, as indicated in Figure 3.4. This causes a change in capacity between the sidewalls of the static and the movable combs.

Since the sensing elements are only a few  $\mu\text{m}^2$  large and in addition with a small displacement amplitude of the seismic mass, the resulting capacitance variation will be very small. Even with an expanded version with several of tens of fingers, the total capacitance is in the order of 0.1 pF [7]. Fortunately, today's measuring techniques are accurate enough to detect capacitance changes in the order of zF ( $10^{-21}$ ) [8].

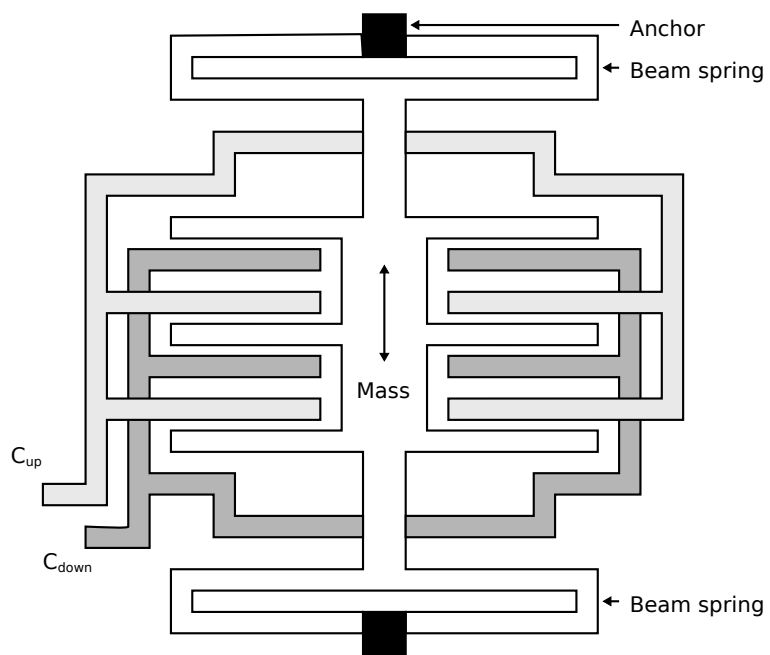


Figure 3.4: Surface micro machined capacitive accelerometer.

## 4 Theory

When a motion, described by  $x(t)$ , continuously changes its direction and  $x(t)$  numerously regain the same quantity, we can define this as an oscillation. A motion that continuously after the time  $T$  repeats, so that

$$x(t) = x(t + T) \quad (1)$$

is valid, we speak of a periodical oscillation. The time  $T$  necessary for one oscillation is defined as period. Its reciprocal quantity

$$f = \frac{1}{T} \quad (2)$$

is the oscillation frequency and describes the number of oscillations per time unit.

### 4.1 Harmonic oscillation

Figure 4.1 shows a model with a movable mass  $m$  which is connected via a linear spring, with the spring constant  $c$ , to a static point. In this simple model the mass moves without any friction. The mass is displaced from its equilibrium position, where the spring is unloaded, along the positive axis with the distance  $x_0$ .

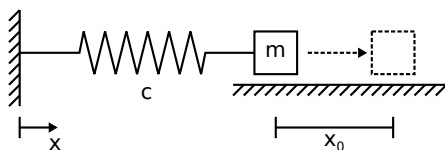


Figure 4.1: Spring-mass-system where the mass is displaced by the distance  $x_0$  along the axis.

When the mass is released there are two forces along the axis acting on the mass, the inertial force of the mass and the retracting force of the spring. The balanced force relationship along the axis is conclusively:

$$m\ddot{x} + cx = 0. \quad (3)$$

This second degree homogeneous linear differential equation with constant coefficients has the general solution

$$x = A \cos\left(\sqrt{\frac{c}{m}} t\right) + B \sin\left(\sqrt{\frac{c}{m}} t\right). \quad (4)$$

The constants A and B are given by the initial values, e. g.,

$$x(t=0) = x_0, \quad \dot{x}(t=0) = 0 \implies A = x_0, B = 0.$$

Hence, the equation to describe the motion of the mass  $m$  is:

$$x = x_0 \cos\left(\sqrt{\frac{c}{m}} t\right). \quad (5)$$

This describes an oscillation with the amplitude  $x_0$  and the oscillation frequency:

$$f = \frac{1}{T} = \frac{1}{2\pi} \sqrt{\frac{c}{m}}. \quad (6)$$

In the physical notation, mechanical oscillations are mainly described by the angular frequency:

$$\omega = \sqrt{\frac{c}{m}}, \quad (7)$$

which only diverge from the frequency  $f$  by a factor of  $2\pi$ .

## 4.2 Free damped oscillations

The type of harmonic oscillation, described in the previous section, is more or less impossible to realize. There is always some form of friction and damping forces present in an oscillating system, causing the amplitude of a free harmonic oscillation to be reduced over time.

In this example we assume a velocity proportional model that develops a resistive force corresponding to  $F = -kv$ , where  $k$  is the damping constant. Figure 4.2 depicts a simple model of an oscillatory system consisting of mass, spring and damper element.

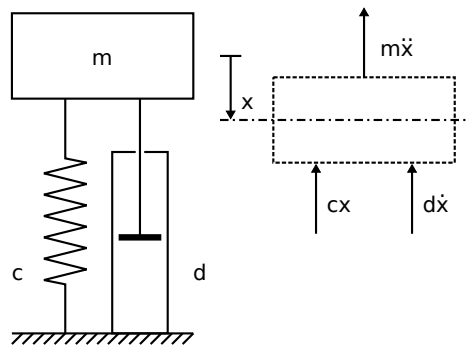


Figure 4.2: Model of a damped spring-mass-system and the acting forces (right).

The coordinate  $x$  describes the distance from the static equilibrium state. The force equation according to Newton's second law of motion follows as:

$$m\ddot{x} + d\dot{x} + cx = 0, \quad (8)$$

which is a linear homogeneous differential equation, assuming that the damping is linear to velocity and the spring force is linear to the displacement distance. By using the dimensionless damping ratio:

$$D = \frac{d}{2\sqrt{mc}}, \quad (9)$$

Equation (8) can be reformulated as:

$$\ddot{x} + 2D\omega\dot{x} + \omega^2x = 0, \quad (10)$$

where the definition of angular frequency  $\omega$  for non-damped oscillations as described in (7) is used. This linear homogeneous differential equation is solved with  $x = C e^{\lambda t}$ , which gives the characteristic equation:

$$\lambda^2 + 2D\omega\lambda + \omega^2 = 0,$$

with the solutions:

$$\lambda_{1,2} = \omega \left( -D \pm \sqrt{D^2 - 1} \right), \quad (11)$$

which can be real or complex depending on the damping values of  $D$ .

For  $D > 1$ , which means strong damping and two separate real poles for  $\lambda$ , the solution can be written as:

$$x = C_1 e^{\lambda_1 t} + C_2 e^{\lambda_2 t} = e^{-D\omega t} \left( C_1 e^{\omega\sqrt{D^2-1}t} + C_2 e^{-\omega\sqrt{D^2-1}t} \right). \quad (12)$$

For the special case where  $D = 1$ , also called critical damping, the solution for  $\lambda$  is a double pole and is described as:

$$x = C_1 e^{\lambda t} + C_2 t e^{\lambda t} = e^{-D\omega t} (C_1 + C_2 t). \quad (13)$$

For both  $D > 1$  and  $D = 1$  there is no oscillation occurring in the system and the  $e$ -term before the bracket results in an asymptotic approach to the resting position.

However, for the case where  $D < 1$  (weak damping and two conjugated complex solutions for  $\lambda$ ) an oscillation does occur, once  $\lambda$  is complex the expression can be rewritten in

cosine and sinus terms (the Euler relation  $e^{iz} = \cos(z) + i \sin(z)$ ), in this particular case as:

$$\begin{aligned} x = C_1 e^{\lambda_1 t} + C_2 e^{\lambda_2 t} &= e^{-D\omega t} \left( C_1 e^{i\omega\sqrt{1-D^2} t} + C_2 e^{-i\omega\sqrt{1-D^2} t} \right) \\ &= C e^{-D\omega t} \cos(\omega_D t - \alpha), \end{aligned} \quad (14)$$

with  $\omega_D = \omega\sqrt{1-D^2}$ .

Out of this result the following conclusions, regarding free damped oscillations, can be drawn:

- With the addition of a damping element the system still has a constant self-resonating frequency. The damped self-resonating frequency is related to the undamped one by:

$$\omega_D = \omega \sqrt{1-D^2} \quad \text{where} \quad \omega = \sqrt{\frac{c}{m}}, \quad (15)$$

meaning that the resulting damped self-resonating frequency is always lower than the undamped one and only depends on the mechanical properties mass, spring constant and damping ratio.

- The oscillation period  $T_D$ , hence, also its reciprocal  $\omega_D$ , can be measured by observing the time span between two amplitude peaks or two points where the function  $x(t)$  crosses the time-axis.
- The time span of one period is always constant, which can be derived using (14):

$$q = \frac{x(t)}{x(t+T)} = \frac{C e^{-D\omega t} \cos(\omega_D t - \alpha)}{C e^{-D\omega(t+T)} \cos(\omega_D(t+T) - \alpha)} = e^{\frac{2\pi D}{\sqrt{1-D^2}}} = \text{constant}. \quad (16)$$

The natural logarithmic decrement  $\Lambda$  is defined as the natural logarithm of  $q$  and has  $D$  as its only variable:

$$\Lambda = \ln q = \frac{2\pi D}{\sqrt{1 - D^2}} \Rightarrow D = \frac{\Lambda}{\sqrt{4\pi^2 + \Lambda^2}}. \quad (17)$$

This means that if the amplitude of two following oscillations can be measured experimentally, it is possible to determine the damping ratio using (17).

In order to understand the magnitude of the eigenfrequency shift due to the introduction of a damping element the following example gives a good picture:

Let us assume that the amplitude of an oscillation is reduced to a half for each period, which can be seen as a relatively large damping. This results, with  $q = 1/0.5 = 2$ , in a logarithmic decrement of  $\Lambda = 0.693$  and a damping ratio  $D = 0.110$ . With equation (15) this leads to an eigenfrequency of

$$\omega_D = \omega \sqrt{1 - D^2} = 0.994\omega.$$

Consequently, if the eigenfrequency of a free damped oscillation is required, the eigenfrequency of the same undamped system is in most cases a very good approximation.

### 4.3 Forced damped oscillations

In the previous case of free damped oscillations the motion of the mass depends only on the initial values (initial displacement and initial velocity). In this section, however, the described oscillation is constantly excited by a force which varies with time, the term forced oscillation is used.

From the force relation, represented in Figure 4.3, the following differential equation can be defined:

$$m\ddot{x} + k\dot{x} + cx = F_0 \cos(\Omega t), \quad (18)$$

with  $F_0$  as applied force and  $\Omega$  as frequency for the oscillating force.

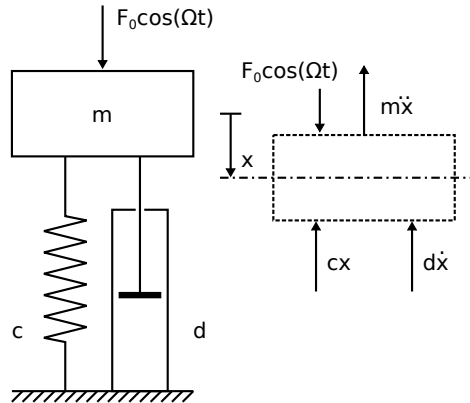


Figure 4.3: Model of a forced damped spring-mass-system, excited by a sinusoidal force.

#### 4.3.1 Oscillations with harmonic excitation of the mass

Using the same notation of symbols ( $\omega$  is the eigenfrequency of the non damped free oscillation and  $D$  the damping ratio), equation (18) can be rewritten as:

$$\ddot{x} + 2D\omega\dot{x} + \omega^2x = F_0 \frac{\omega^2}{c} \cos(\Omega t). \quad (19)$$

The differential equation is a linear non homogeneous one, with a solution composed of a homogeneous part  $x_{\text{hom}}$  and particular part  $x_{\text{part}}$  :

$$x = x_{\text{hom}} + x_{\text{part}}. \quad (20)$$

The equation for solving  $x_{\text{hom}}$  is identical with the differential equation (8), hence, the solution is the same as in (14). As for the particular solution the following equation is assumed:

$$x_{\text{part}} = A \cos(\Omega t - \phi), \quad (21)$$

and then inserted in (19). Which produces:

$$\begin{aligned} & \left( -F_0 \frac{\omega^2}{c} - A\Omega^2 \cos \phi + 2AD\omega\Omega \sin \phi + A\omega^2 \cos \phi \right) \cos(\Omega t) \\ & + \left( -A\Omega^2 \sin \phi - 2AD\omega\Omega \cos \phi + A\omega^2 \sin \phi \right) \sin(\Omega t) = 0. \end{aligned}$$

This relationship can only be valid (for every  $t$ ) when both expressions in the parentheses equals zero. By setting the second expression to zero, the relationship

$$\tan \phi = \frac{2D\omega\Omega}{\omega^2 - \Omega^2} = \frac{2D\Omega/\omega}{1 - (\Omega/\omega)^2} \quad (22)$$

is obtained. By doing the same with the first expression and inserting the result in (22), a relationship for the amplitude  $A$  can be formulated:

$$A = \frac{F_0/c}{\sqrt{(1 - (\Omega/\omega)^2)^2 + 4D^2 (\Omega/\omega)^2}}. \quad (23)$$

The solution is thereby complete. Both  $x_{\text{hom}}$  and  $x_{\text{part}}$  can be described with a cosine function and the solution can therefore be visualized as two overlapped oscillations (see Figure 4.4). However, if the homogeneous part  $x_{\text{hom}} = Ce^{-D\omega t} \cos(\omega_D t - \alpha)$  is examined closer we can see that, due to the exponential part with negative exponent, this part will decrease towards zero the larger  $t$  gets and the final solution is the particular solution. The particular solution is a purely harmonic oscillation with the same frequency as the forced oscillation and with a constant amplitude. Consequently, a forced oscillation of a damped system (assuming that the mass is excited by a force) will always, regardless if  $\omega > \Omega$  or  $\omega < \Omega$ , after a certain time oscillate with the excited frequency  $\Omega$  and with a constant amplitude.

This is defined as the stationary solution:

$$x_{st} = \frac{F_0/c}{(1 - \eta^2)^2 + 4D^2\eta^2} \cos(\Omega t - \alpha) \quad (24)$$

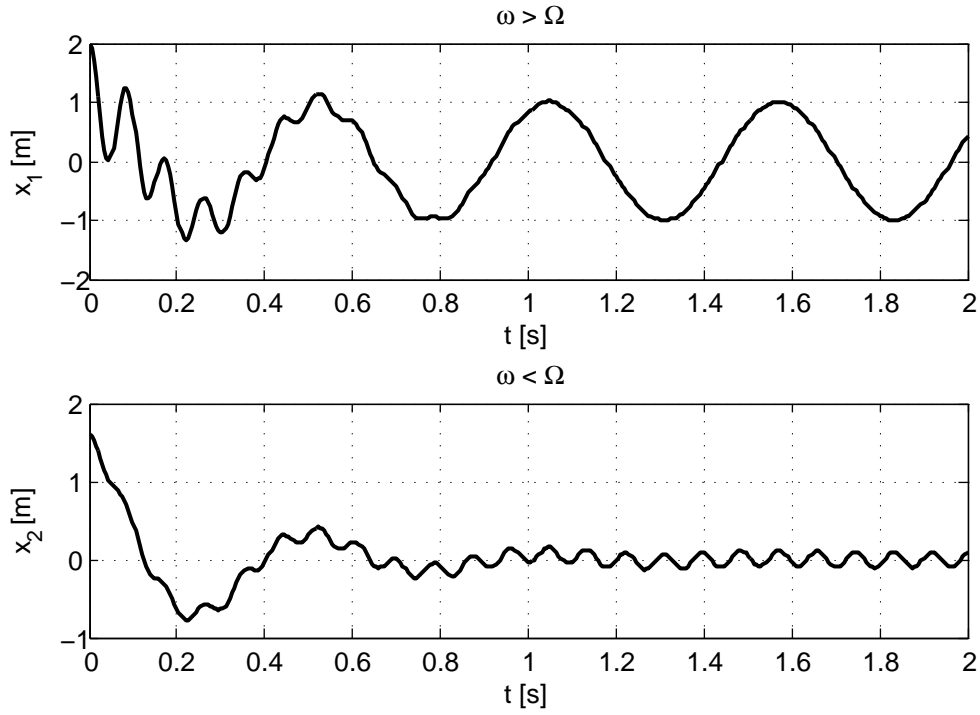


Figure 4.4: Two examples of the homogeneous and the particular solution added together.

where:

$$\eta = \frac{\Omega}{\omega} = \frac{\Omega}{c/m}. \quad (25)$$

The phase shift  $\alpha$  in (24) can be calculated with

$$\tan \alpha = \frac{2D\eta}{1 - \eta^2}, \quad (26)$$

where  $D$  is the damping ratio, described in (9).

Some conclusions can be made by looking at (24):

- The term in front of the cosine function in (24) represents the stationary amplitude.

In the numerator of the fraction, which defines the size of the amplitude, stands  $x_{static} = F_0/c$  describing the displacement of the spring when it is loaded by a static force  $F_0$ . For very small excitation frequencies the denominator of the fraction results in a value of approximately 1, hence the oscillation amplitude is approximately as large as for the static case.

- For an arbitrary excitation frequency  $\Omega$  the amplitude (normalized with the static displacement) is described by the transfer function

$$V(\eta) = \frac{1}{\sqrt{(1 - \eta^2)^2 + 4D^2\eta^2}}. \quad (27)$$

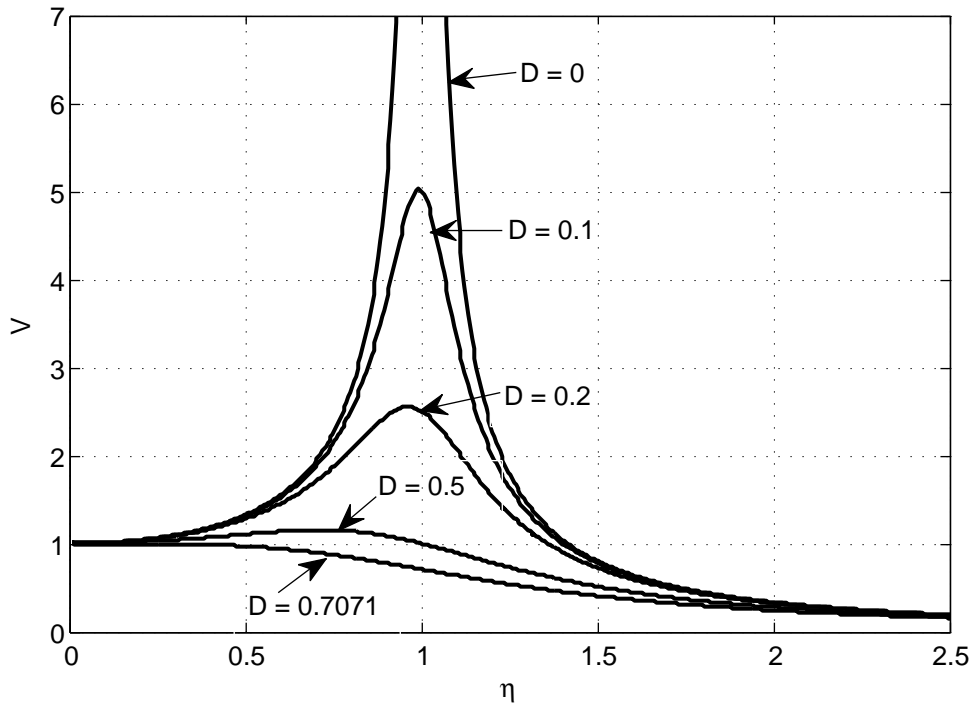


Figure 4.5: Transfer function of a damped spring-mass-system, where the mass is excited with a harmonic force.

The following conclusions can be drawn by looking at Figure 4.5, which shows the transfer function  $V(\eta)$  for different damping ratios:

- For very small damping ratios the transfer function exhibits very large values around  $\eta = 1$  (for  $D = 0$  the function has a pole at  $\eta = 1$ ). An excitation with a frequency  $\Omega$ , which corresponds to the eigenfrequency of the undamped system, results in very large amplitudes if the damping is low (resonance).

- The relative maximum of the transfer function is located before the point  $\eta = 1$ . No resonance behavior occurs for damping values greater than  $D = 1/\sqrt{2} = 0.707$ .

### 4.3.2 Harmonic excitation of the foot point of the spring or of the damper

In the example, depicted in Figure 4.6, the spring of the system is displaced in a harmonic manner. This displacement results in a force on the mass proportional to the change in spring length. The balanced force equation along the vertical axis is:

$$m\ddot{x} + k\dot{x} - c(x_0 \cos(\Omega t) - x) = 0,$$

which can be reformulated, using the previous notations, to:

$$\ddot{x} + 2D\omega\dot{x} + \omega^2 x = x_0\omega^2 \cos(\Omega t). \quad (28)$$

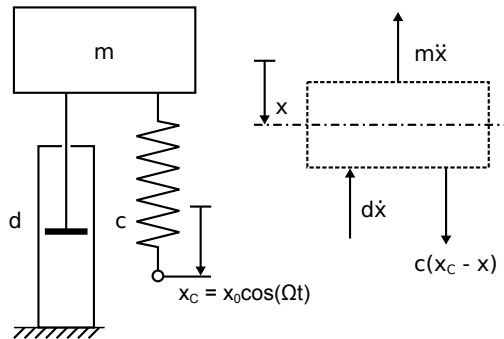


Figure 4.6: Model of a forced damped spring-mass-system, where the spring foot point is excited by a harmonic displacement.

This differential equation has the same form as (19). By substituting  $x_0 = F_0/c$  the same results can be applied so that an oscillation system where the spring foot point is displaced by  $x_c = x_0 \cos(\Omega t)$ , the stationary solution

$$x_{st} = x_0 V(\eta) \cos(\Omega t - \alpha) \quad (29)$$

is obtained. Where  $\alpha$  is the phase shift according to (26) and  $V(\eta)$  is the function according to equation (27).

When only the damper foot point instead is excited by a harmonic displacement, as depicted in Figure 4.7, the balanced force equation is:

$$m\ddot{x} - k(\dot{x}_D - \dot{x}) + cx = 0.$$

Which result in the differential equation

$$\ddot{x} + 2D\omega\dot{x} + \omega^2x = -2D\eta x_0\omega^2 \sin(\Omega t).$$

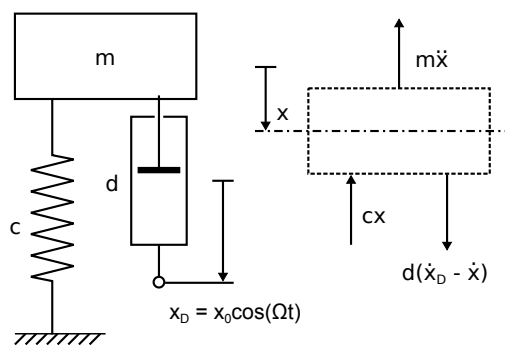


Figure 4.7: Model of a forced damped spring-mass system, where the damper foot point is excited by a harmonic displacement.

By using the same solving method as in the Chapter 4.3.1, it is found that an oscillator where the damper foot point is displaced by the relationship  $x_D = x_0 \cos(\Omega t)$ , has the stationary solution

$$x_{st} = -2D\eta x_0 V(\eta) \sin(\Omega t - \alpha) = -x_0 V_D(\eta) \sin(\Omega t - \alpha). \quad (30)$$

Where  $\alpha$  is the phase shift between the applied and resulting oscillation, which can be calculated with (26), and the transfer function  $V_D$  which can be calculated with (27):

$$V_D(\eta) = 2D\eta V_D(\eta) \quad (31)$$

When the system is excited with the same harmonic displacement on the spring foot point and on the damper foot point (see Figure 4.8), the stationary equation can be formulated as a combination of the equations (29) and (30) due to the linearity of the differential equations:

$$x_{st} = -x_0 V(\eta) [\cos(\Omega t - \alpha) - 2D\eta \sin(\Omega t - \alpha)], \quad (32)$$

which can be reformulated so that amplitude and phase shift are easier to recognize:

$$x_{st} = -x_0 \sqrt{1 + 4D^2\eta^2} V(\eta) \cos(\Omega t - \bar{\alpha}) = x_0 V_S(\eta) \cos(\Omega t - \bar{\alpha}). \quad (33)$$

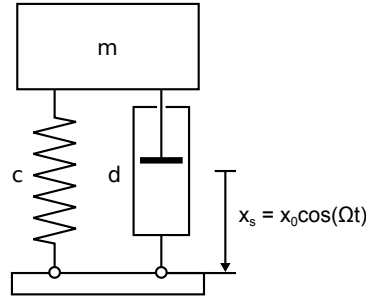


Figure 4.8: Model of a forced damped spring-mass-system where the spring as well as the damper foot point are excited with a sinusoidal displacement.

Hence, the transfer function for the case where spring and damper are excited with the same harmonic displacement is:

$$V_S(\eta) = \sqrt{1 + 4D^2\eta^2} V(\eta), \quad (34)$$

and the phase shift, which deviates from the previous cases, as follows:

$$\tan \bar{\alpha} = \frac{2D\eta^3}{1 - \eta^2 + 4D^2\eta^2}. \quad (35)$$

Figure 4.9 depicts the two cases damper footpoint and damper-spring footpoint excitation

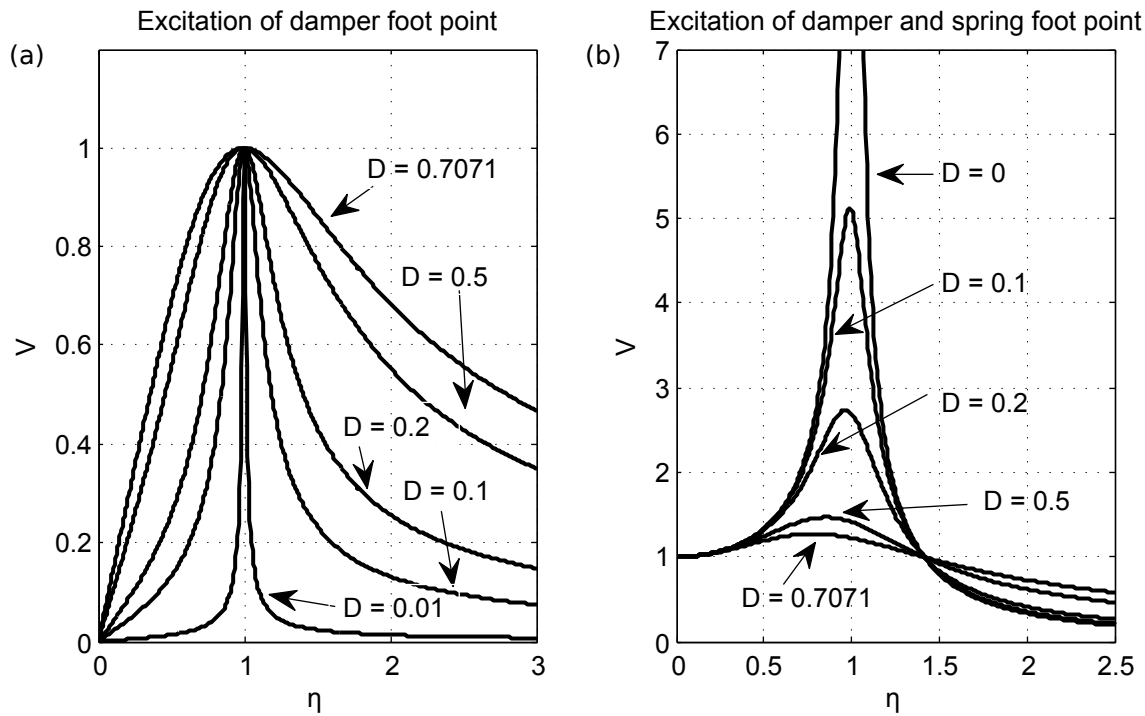


Figure 4.9: Transfer functions of a damped spring-mass-system, where a) the damper b) the damper and spring footpoints are excited.

## 5 Vibration Sensor

The sensor is designed in a way that it can easily be attached onto an object and thereby measure the corresponding vibrations. The expected vibrations will have a maximum frequency of 15 kHz and displacements in the micron range. The sensor size is limited to an area of 2 mm<sup>2</sup>. When the sensor is placed on an object it will, due to the additional weight, influence the original vibration amplitude. Hence, to maximize the total vibration amplitude, and accordingly the strength of the sensors output signal, the mass of the sensor has to be kept as low as possible, especially in the case of small sample objects.

The working principle of the sensor is a spring–mass–system where a freestanding mass is attached by a set of springs. Around this seismic mass there is a solid frame, on which the springs are fixed. The displacement of the mass is measured by the capacitive change between the movable mass and the static parts of the sensor.

### 5.1 Sensor design

The entire sensor is made of silicon, using MEMS (MicroElectroMechanical Systems) techniques. Silicon is elastic to a degree, that makes the production of very thin and long springs possible. This also allows to place electronics and sensor(s) to one and the same chip. The basic design principle can be seen in Figure 5.1, which shows the sensors footprint.

Mass and springs are formed out of a thin silicon layer by selectively removing parts (light gray areas in Figure 5.1) of the plate. Once the mass is freestanding, it is movable but held by the two springs. The mass is mainly displaced along the  $x$ -axis and this displacement is what the sensor is designed for to register. To form a capacitive sensing system, the frame and mass are equipped with sets of sensing combs (see Figure 5.5). Each of these sets acts as a variable parallel plate capacitor.

The desired resonance frequency is the starting point for the design of the different test sensors. Mass and spring stiffness of the system are the only two factors that determine the resonance frequency (there is only a slight influence of the damping coefficient) and can therefore be tailored to achieve a specific resonance frequency.

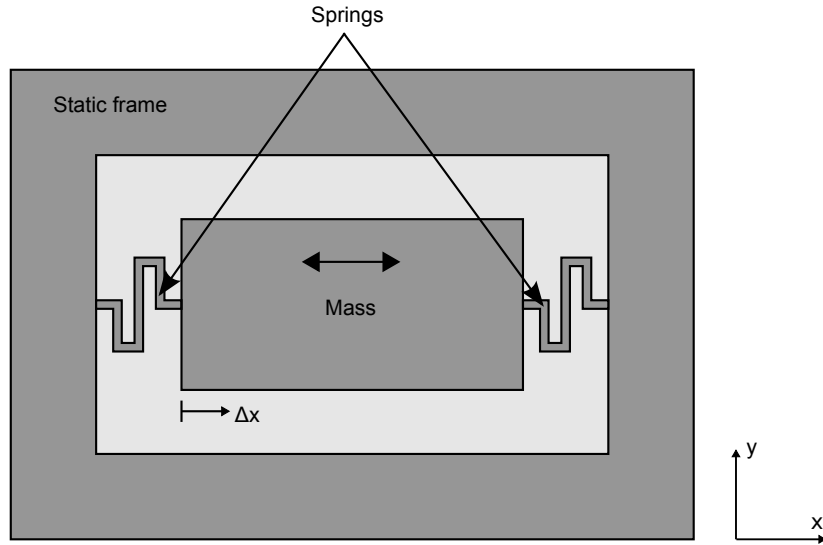


Figure 5.1: Basic design of a vibration sensor.

### 5.1.1 Mass

The mass is determined by the geometric dimensions of the seismic mass (Figure 5.1), the thickness is already fixed by the choice of wafer.

### 5.1.2 Spring

The spring element consists of a set of folded beams. The stiffness of one beam element, with a rectangular cross section, can be described as [9]:

$$k_x = \frac{3E_x I_z}{L^3} = \left[ I_z = \frac{tw^3}{12} \right] = \frac{E_x tw^3}{4L^3}, \quad (36)$$

where  $E_x$  is the Young's modulus in the  $x$ -axis of a (100) silicon wafer,  $I_z$  the moment of inertia around the  $z$ -axis and  $L$  the length of the beam.

An example of a folded spring element is depicted in Figure 5.2 a) and its corresponding spring model in c). The individual beams act as springs in series, hence:

$$k_{spring} = \frac{1}{\frac{m}{k_s} + \frac{n}{k_L}}, \quad (37)$$

where  $m$  is the number of short beams and  $n$  the number of long beams. Note that the parts adjoining the beams are discarded in the spring constant calculation since they are considered to be considerably stiffer than the beams.

The total spring stiffness of the sensor is  $k_{sensor} = 2k_{spring}$  since every sensor has one spring on each side of the proof mass that acts as two springs in parallel.

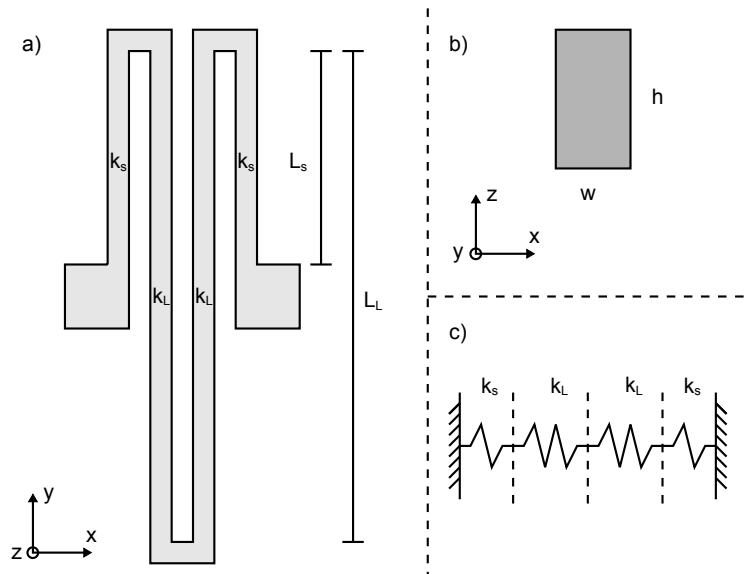


Figure 5.2: a) One spring element. b) Cross section of one spring beam. c) Equivalent spring system.

In conclusion, the stiffness of the spring(s) can be picked by choosing beam width, length and number of beams.

### 5.1.3 Capacitance

The capacitance of the sensor can be described by:

$$C = \frac{\epsilon A}{d}, \quad (38)$$

where  $\varepsilon$  is the permittivity,  $A$  the face area of the capacitor and  $d$  the distance between two combs. In this case  $A$  is the total area of one set of static combs facing a set of fingers,  $d$  is the distance between a static finger and finger of the mass.

A model of this capacitor is depicted in Figure 5.3 and the relative capacity change can be described as:

$$\Delta C_{rel}(x) = \frac{x}{d_0 - x}. \quad (39)$$

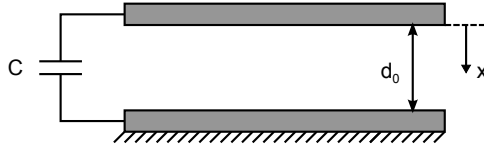


Figure 5.3: Single plate capacitor.

The equation shows a nonlinear dependence of  $x$ , which in sensing is a disadvantage. For this reason, the top and bottom comb pairs (see Figure 5.5) are mirrored so that a  $x$ -axis displacement results in an equal amount of positive and negative plate separation. This set-up is a differential plate capacitor and is depicted in Figure 5.4 and the relative capacity is now:

$$\Delta C_{rel}(x) \approx \frac{2x}{d_0}. \quad (40)$$

This is an approximation of the capacity change for small deflections. The sensor is designed to sense vibration amplitudes that are less than 1% of the gap distance, which makes the approximation valid.

Since the deflection is so small, it is desirable to maximize capacity during operation to more easily obtain a high signal to noise ratio. This can be achieved by increasing the area of the total face surface by making sure that each individual surface area is as large as possible, i. e, long and high combs. Large number of comb pairs also maximizes the total area. A larger capacitive change is also achieved by producing sensors with a small equilibrium distance between the face areas.

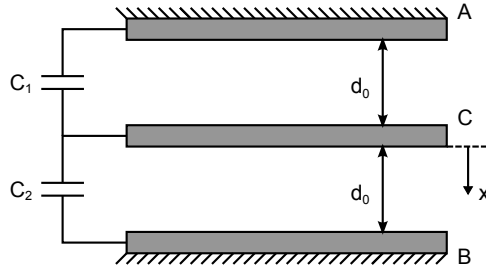


Figure 5.4: Differential capacitor. A, B and C denotes the sensor sections marked in Figure 5.5.

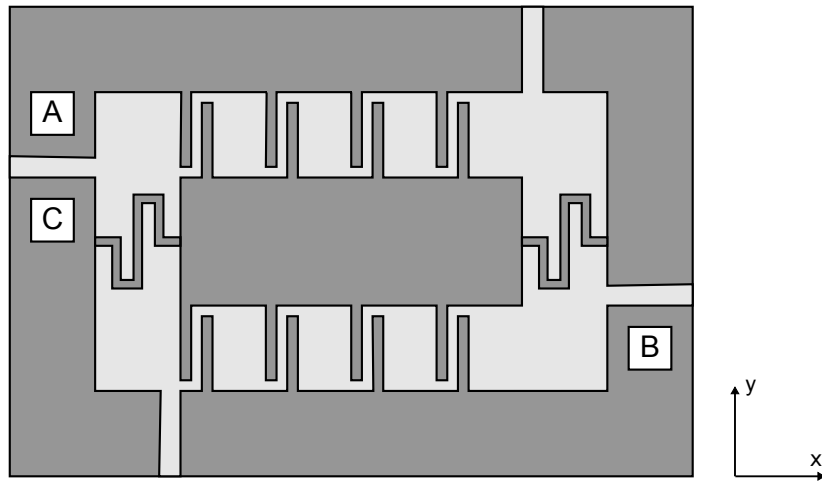


Figure 5.5: A detailed representation of the freestanding mass sensor design.

Another method of achieving a large output signal is taking advantage of the resonance of the a mass-spring system. If the system is resonating, the displacements are increased by the quality factor, which generates a higher output signal. This advantage of larger displacements is only valid within a limited frequency span.

A simplified model for the resonance frequency of this spring-mass-system (an extensive

model is found in Chapter 4) can be described as:

$$\omega_0 = \sqrt{\frac{k}{m}}, \quad (41)$$

where  $\omega_0$  is the resonance frequency,  $k$  the spring stiffness and  $m$  the mass. This model does not take into account the mass of the springs or the electrostatic forces of the capacitive read-out.

## 6 Production of Test Sensor

The test sensor is produced out of the substrate part of a SOI-wafer. The sensor elements will be formed using a plasma etch. To be able to create a freestanding proof mass and springs, a cavity is (wet) etched out from the opposite side of the wafer. The finished product will not be electrically operational but is manufactured to primarily characterize the mechanical properties.

### 6.1 Preparation

The wafer used for the production have a diameter of 100 mm, a (100) crystal orientation, a thickness of 350  $\mu\text{m}$  and are polished on both sides. The wafers are delivered with a sandwich of LPCVD (Low Pressure Chemical Vapor Deposition) silicon nitride ( $\text{Si}_3\text{N}_4$ ) layer and a thermally deposited silicon oxide ( $\text{SiO}_2$ ) layer on both sides (see Figure 6.1). In the device fabrication, the nitride layer acts as a mask for the etch step of the backside cavities. The nitride/oxide layer on the other side is removed by plasma etching which results in a smooth Si surface. It is on this side, where the sensor structure as well as the metal layer will be fabricated. The nitride/oxide layer on the other side of the wafer is protected by a 1.2  $\mu\text{m}$  resist layer (type AZ1512) to avoid any etching during the plasma process.

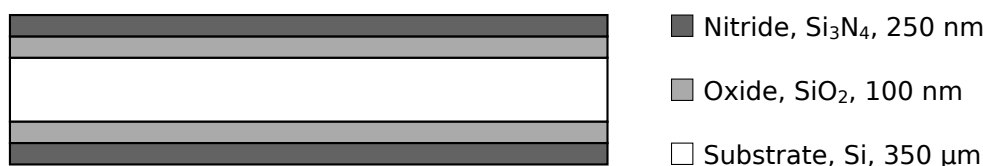


Figure 6.1: Cross section of silicon nitride coated wafer.

### 6.2 Coating layer removal

Since the isolation is a sandwich of two materials ( $\text{Si}_3\text{N}_4 + \text{SiO}_2$ ) a combined plasma process is used, first with  $\text{CF}_4/\text{O}_2$  gas mixture and then switched to a  $\text{CHF}_3/\text{O}_2$  gas mixture. Theoretically, the  $\text{CF}_4$  process can be applied for both materials, but the selectivity of

CF<sub>4</sub>/O<sub>2</sub> plasma to Si is very poor and would result in a rough Si surface [10]. A smooth surface is required for a well executable lift-off process.

The exact etch rates of Si<sub>3</sub>N<sub>4</sub> and SiO<sub>2</sub> differ from experiment to experiment. Therefore, tests are made with test wafers to determine the etch rates and thereby removing the Si<sub>3</sub>N<sub>4</sub> and SiO<sub>2</sub> layers of the production wafers correctly. The wafer is specified as follows:

	<b>Production wafer</b>
Diameter	100 mm
Si <sub>3</sub> N <sub>4</sub> thickness	250 nm
SiO <sub>2</sub> thickness	100 nm

Table 1: Wafer specifications

### 6.2.1 Coating layer removal

In the first test to remove the coating a plasma etching with CF<sub>4</sub>/O<sub>2</sub> gas mixture is conducted. After 5 minute etching both layers (Si<sub>3</sub>N<sub>4</sub>, SiO<sub>2</sub>) were removed, being confirmed by the color (gray) of the wafer surface as well as the electrical conductivity. The plan was to use the CF<sub>4</sub>/O<sub>2</sub> plasma mixture only for the Si<sub>3</sub>N<sub>4</sub> layer to reduce etching of the Si wafer (as described above). By using a 5 min CF<sub>4</sub>/O<sub>2</sub> plasma mixture, however, both layers were removed and consequently the Si layer was attacked. The CF<sub>4</sub> etch had to be accordingly shorter than 5 minutes to avoid damaging the Si surface.

For the second test wafer, a combined etch process is tested. After 3 minute CF<sub>4</sub> plasma etching the topmost Si<sub>3</sub>N<sub>4</sub> layer was fully removed, confirmed by the wafer surface color (blue for the SiO<sub>2</sub> layer, the color depends mainly on the thickness of the layer). Subsequently, a 3 minute CHF<sub>3</sub>/O<sub>2</sub> etching completely removed the remaining SiO<sub>2</sub>/O<sub>2</sub> layer, once again confirmed by the color (gray). These etch times successfully removed both layers without harming the Si surface and were used on the actual test wafers.

During the plasma etch, polymers are created which are deposited onto the sample surface. The polymer contaminations are removed with a 10 minute O<sub>2</sub> plasma etch.

### 6.2.2 Removal of SiO<sub>2</sub> to form ohmic conducts

A surface of pure Si exposed to air naturally forms a thin layer of SiO<sub>2</sub>. However, during a plasma etching with O<sub>2</sub>, the oxidation reacts deeper into the material, forming a thicker oxidation layer, a so called "hot layer". This layer is unwanted since it decreases the conductivity of metal conducts. The production wafer has a hot SiO<sub>2</sub> layer since O<sub>2</sub> was used as a cleaning method in the last step in the previous combined plasma etch. The layer is removed by etching with hydrofluoric acid (HF) with a concentration of 1%. The selectivity of HF to SiO<sub>2</sub> is very high leading to practically no effect on the Si surface.

## 6.3 Structuring the metal layer

The test sensors are produced to characterize harmonic motion. The deposition of a metal layer might therefore seem redundant. However, by performing as many as possible of the production steps for an electrically functional sensor, possible future problems or errors might be precluded. Also, the metal layer pattern is used as a tool for aligning the wafer during the backside lithography step for the cavity.

The metal layer is structured with lift off technique. First, a layer of resist is applied with a pattern for the position of the contact pads. Then a metal film is deposited on top of the sacrificial resist layer. Finally, the sacrificial layer is dissolved, leading to a patterned metal film. If a conventional resist would be used for this process the edges of the resist will take a form as depicted in Figure 6.2. During deposition of the metal film on such a resist pattern, also the side walls of the resist are slightly covered (Figure 6.2). When removing the sacrificial layer, the metal film will be lifted off and the correct pattern of contacts will be produced. However, during this process, the metal film will be ripped off, resulting in uneven edges of the metal film. To avoid this effect, an image reversible resist has to be chosen.

An image reversible resist is a positive resist with the unique ability to change selectivity to the developer by UV-light exposure followed by thermal processing. The image reversible process flow starts by exposing those areas, with UV-light, where the metal film should not be located (see Figure 6.3). The resist is a positive type and yet the areas where a sacrificial layer has to be kept are exposed. That means, if the wafer is developed at this stage, the exposed areas would be dissolved.

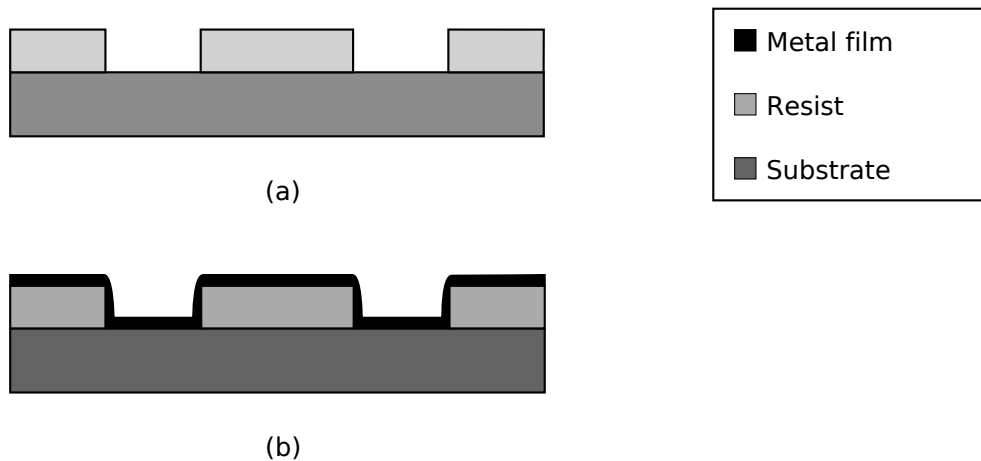


Figure 6.2: Metal layer deposition on a conventional resist. (a) Cross section of a conventional resist after development. (b) Schematic cross section after metal film deposition on a conventional resist layer.

However, by heating up the resist ( $> 110^{\circ}\text{C}$ ) [11], the character of the areas exposed to UV-light are changed. Namely, the resist is polymerized by the heating, making it more resistant to the developer. These areas on the wafer (exposed by UV-light) are now permanent and will not be affected by further heating or light exposure.

The areas of the resist which should be removed, are still unaffected by the process steps so far. By exposing the whole wafer to UV-light, these areas will get sensitive to the developer. After rinsing the wafer with the developer, the resist pattern has the form as shown in Figure 6.3. The resist side walls now slanted away from the intended metal film area.

During the metal evaporation process, the slanted edges will not be covered (Figure 6.3) and no metal layer has to be ripped off during the lift-off process. The same type of slanted walls can be achieved by using a negative resist. When the negative resist is developed the exposed areas take on a polymeric composition and can not be solved by a solvent. To strip the negative resist an oxygen plasma process has to be used, which excludes an effective lift-off process. Positive resist, however, can be dissolved with a liquid solvent (acetone), which better accesses the sacrificial resist layer.

The end result can be seen in Figure 6.3. The material gold is chosen due to its high

conductivity and compatibility to wire bonding. However, gold does not adhere well on the silicon surface. Chromium on the other hand is compatible with both materials due to matching crystal lattice type. Chrome is therefore used as an adhesion layer between gold and silicon. A 50 nm thick chrome layer is deposited by electron beam evaporation, followed by a 100 nm thick gold layer deposited by thermal evaporation.

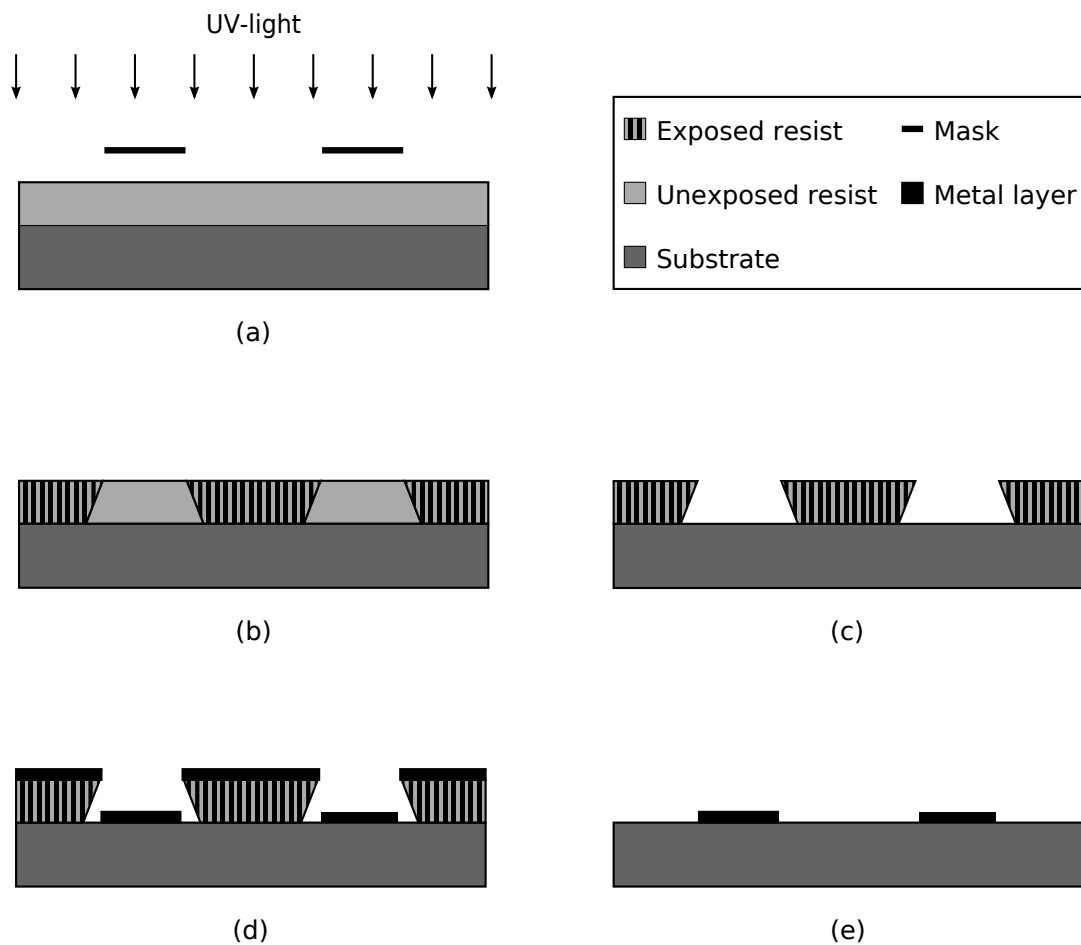


Figure 6.3: Production steps for metal layer deposition using image reversible resist. (a) Cross section of the wafer during UV-light exposure, (b) after UV-light exposure, (c) with processed image reversible resist, (d) with evaporated metal film, (e) final result of the lift-off process.

## 6.4 Backside cavity

As mentioned in Section 6.1 the remaining nitride/oxide layer will act as a mask. To form this mask, the nitride/oxide layer has to be etched with a plasma process. Since the patterned metal layer is already positioned on the top side of the wafer, the mask has to be aligned to this pattern. To achieve this, a double side mask aligner is used where one can observe both sides of the wafer simultaneously.

After the photolithography for the nitride mask pattern, the  $\text{Si}_3\text{N}_4 + \text{SiO}_2$  layer is etched with the same type of plasma process as for the nitride layer strip (see section 6.2). A 5 minute  $\text{CF}_4/\text{O}_2$  etch, followed by a 5 minute  $\text{CHF}_3/\text{O}_2$  etch is conducted (in regard to a 3 + 3 minute etching for the nitride layer strip on the top side of the wafer).

For the fabrication of the back side cavities a hot 30 wt% KOH etchant is used. This type of solution is very aggressive to silicon. The other side of the wafer, where the freestanding structures will be produced, may not be affected by KOH in this step since that would result in a rough surface. Therefore, the handle layer is protected by a special resist and a wafer holder for etching. The wafer holder is clamping the wafer so that only one side (the backside) is exposed whereas the other side (top side) is isolated by an O-ring.

The etch rate of KOH on silicon depends on the crystal orientation. For instance the etch rate ratio between a (100) and a (111) plane is 400:1. Hence, an etching with KOH will produce slanted side walls along the (111)-plane, with an angle of  $54.7^\circ$ [12]. This has to be taken into account for in the design of the backside mask (see Figure 6.4).

The etch rate also depends on the dopant type, the dopant concentration in the substrate, the KOH concentration and the KOH temperature.

The resistivity of the handle wafer is  $<0.01 \Omega\text{cm}$ , the KOH concentration is 30 wt% and the temperature is  $80^\circ\text{C}$ . With these parameters the etch rate is approximately  $1 \mu\text{m} / \text{min}$ . The thickness of the handle wafer is  $350 \mu\text{m}$  and the sensor structure is designed to be  $20 \mu\text{m}$ , hence an etching time of approximately 5.5 h is required.

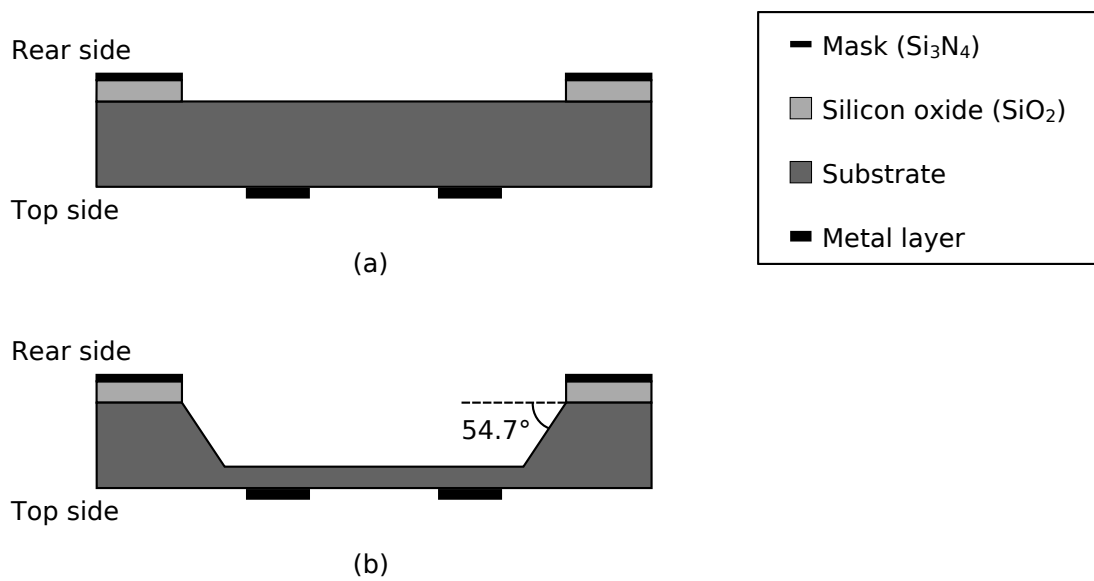


Figure 6.4: Backside cavity etch process. (a) Cross section after the backside etch. (b) The result after the backside cavity etching.



## 7 Micro System Analyzer

To measure and evaluate the vibration characteristics for the shaker and the sensor prototypes, a Micro System Analyzer (MSA, Polytec) was used. This system is based on a microscope and combines three different measuring modes in one set-up. The system is able to measure vibrations as well as 3D geometries by means of these modes:

- out-of-plane measurement (scanning laser vibrometry),
- in-plane measurement (stroboscopic video microscopy) and
- topographical measurement (white light interferometry).

The set-up for a measurement, in either one of these modes, is carried out by a PC with a software provided by Polytec. The specific measurement parameters are set within the software program. Via the program, the user can also inspect the optical part of the set-up through a live camera feed. The basic optical adjustments are, however, operated with analog dials on the side of the MSA microscope head (see Figure 7.1), just like a conventional microscope. The resulting measurement data is gained by the software, where it is evaluated and, finally, visually presented in the program.

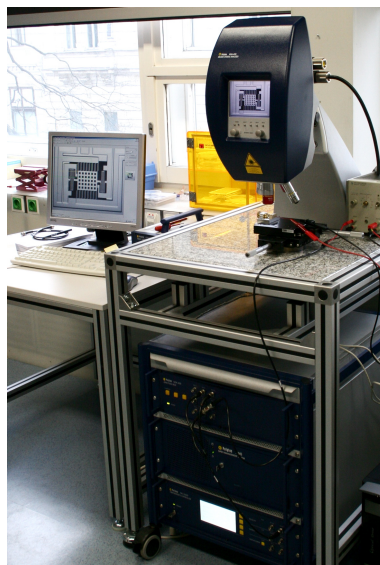


Figure 7.1: Image of the Micro System Analyser (MSA).

## 7.1 Out-of-plane measuring mode

The out-of-plane mode uses a monochromatic light source, namely a laser beam with a wavelength of 633 nm. It is used to measure the displacement amplitude and frequency of a vibrating object by monitoring the Doppler shift. The basic measuring principle is depicted in Figure 7.2. If the specimen is moving/vibrating, the resulting reflection of the laser beam will have a different frequency than the original signal. In the MSA-system, the laser beam is first slit into two beams where one is the measuring beam and the other the reference beam. During a measurement the reference beam is pointed to a static part of the specimen. The two beams are routed to a interferometer to detect frequency shifts. The Doppler frequency can be described as [13]:

$$f_D = v \frac{2}{\lambda}, \quad (42)$$

where  $f_D$  is the Doppler frequency,  $v$  is the velocity of the moving target and  $\lambda$  is the wavelength of the applied monochromatic light.

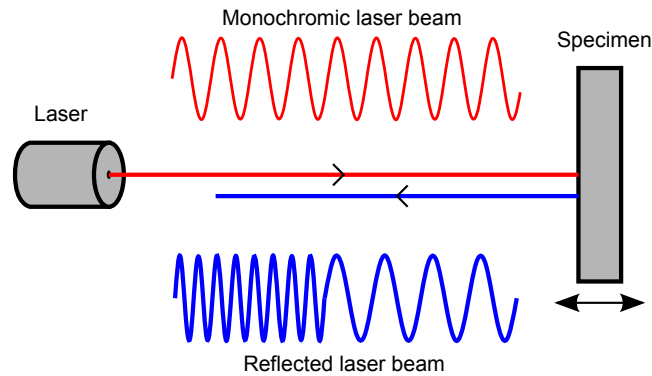


Figure 7.2: Working principle of the laser interferometry mode, utilizing the Doppler effect.

Hence, the frequency shift is proportional to the velocity of the measured object. In this case the Doppler frequency is known for the specific laser ( $f_D = 3.16 \cdot 10^6$  Hz), hence, the only unknown variable is the velocity. Consequently, this provides the great advantage of that no calibration of the device is required since the constant of proportionality is well known.

A measurement is conducted through the PC-program, where a live feed from the camera is shown. On top of this feed an overlay with one or more measuring points is defined. In the case of multiple measuring points, a mesh can be formed to create a surface representation of the vibrations. Before a measurement is started, various parameters are inserted (e. g. bandwidth, number of FFT-lines, exciting signal etc.) and the reference laser beam is positioned, preferably, onto a static part of the specimen. Once the measurement is started the scan laser beam is automatically positioned to one of the predefined measure points and the chosen exciting signal is applied. This process is repeated until every measure point is covered.

The gathered result for every measure point is processed and linked together by the software so it can be presented by an animated 3d-surface of the vibration. This mode is the most accurate and the quickest of the three MSA-modes with a resolution of the oscillation amplitude of a few pm.

## 7.2 In-plane measuring mode

The in-plane measuring mode uses the same camera as for the live feed to record periodic displacements of an oscillating specimen. The device can record vibration frequencies up to 1 MHz. The camera itself features only a frame rate of 15 fps, making a registration of a 1 MHz displacement frequency impossible. This is solved by applying short pulses of light, using an LED. Although the sensor registers all incoming light over a "long" period of time, only the state of the specimen during the short flash is recorded since the flash is significantly brighter than the ambient light. In order to produce a picture bright enough, multiple pulses of light can be applied in the same frame by synchronizing the flash at exactly the same phase values of the excitation signal. An example can be seen in Figure 7.3 where the specimen is exposed with three light pulses per frame. Each of these frames are recorded and saved by the software as a series of pictures.

Figure 7.4 shows an example of two recorded pictures. The software performs a pattern recognition algorithm to find similarities between the two pictures and thereby calculates the displacement, in  $x$ - and  $y$ -axis, respectively. This is repeated for each picture set, resulting in a displacement representation for the whole oscillation cycle. Before a measurement is started, the user has to define an area of the camera view where pattern recognition should be applied. It is recommended for the user to choose an area with high

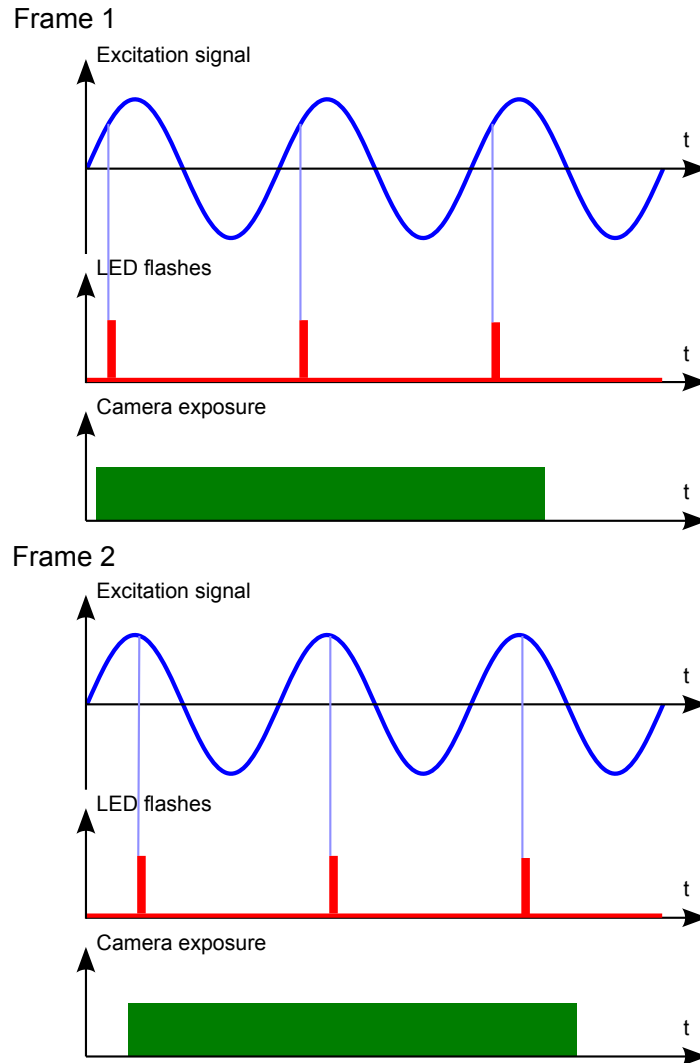


Figure 7.3: Example of an exposure cycle for measuring in-plane displacement using a series of LED flashes.

contrast regions, such as edges, to ease the recognition process and get more accurate results.

The evaluated data can be inspected in graph form, as raw data or as a movie clip.

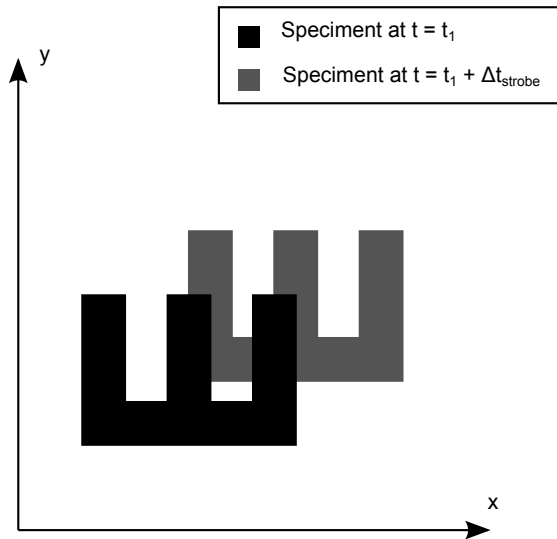


Figure 7.4: Example of two consecutive exposures of an arbitrary vibrating specimen.

### 7.3 Topographical measuring mode

The topographical feature of the MSA-system allows height measurements of an object. The measurement is non tactile and the specimen is scanned by moving the microscope objective perpendicular to the sample. It uses light which is reflected on the sample and subsequently run through an interferometer. The resulting correlogram signal indicates the correct height value on that point where maximum intensity occurs. One correlogram and subsequently the related height value is simultaneously sampled for each pixel of the CCD camera. The software then generates a 3D-topographical representation of the specimen.

Figure 7.5 illustrates an example of a topographical measurement. The interference objective used in the MSA is of Mirau type, meaning that the reference mirror is located on one of the objective lenses [14]. When the distance between reference mirror and the transparent mirror is the same as between the transparent mirror and an area on the specimen, constructive interference occurs and the height value is recorded. The set-up features a vertical scanning range of 250  $\mu\text{m}$  with a resolution of 200  $\mu\text{m}$ .

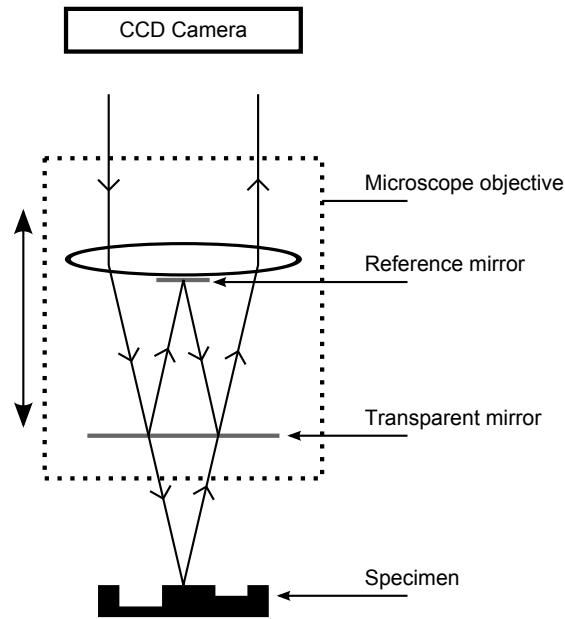


Figure 7.5: Simplified model of the topographical measurement mode of the MSA using a Mirau objective.

## 7.4 Area of use for each mode

In this thesis all three measuring modes will be used. The topographical mode will be used to verify the manufacturing quality of the sensor. This mode is useful if, for instance, a particular sensor refuses to oscillate. A topographical image could identify possible contaminations or stiction.

The in-plane mode is used to characterize the different sensors. This mode is the slowest and most memory demanding of the three. It is therefore, preferably, only used in a small frequency window around the frequency point of interest. In this case the point where the resonance peak of the sensor is located. For instance a full frequency sweep (0-15 kHz) with a high resolution (10 Hz step size) takes more than 10 hours.

The out-of-plane mode, on the contrary, is fast and extremely accurate. The downside is that it can only perform out-of-plane measurements. Making this mode incompatible to characterize the frequency response of the (in-plane moving) sensor prototypes. It is, however, useful for the characterization of the test environment.

## 7.5 Automation scripts

For the specific task of characterizing the testing environment as well as the sensor prototypes, the Polytec software was tailored by creating different scripts for extracting raw data. These scripts serve to automate the measuring process and to evaluate the data in a common environment. The exported data sets is processed and presented using MATLAB because of its power of handling data sets and matrices. Another advantage, utilizing the export scripts, is the disk storage issue. For instance, a in-plane measurement typically takes up somewhere between 100 MB to 10 GB of disk space. Whereas the extracted data, important for the characterization, takes up less than 10 MB.

### 7.5.1 In-plane automation script

The motivation to write a script in the first place was one small limitation in the Polytec software. There is only the possibility to export and save measured data as a text file. The problem, however, is that only displacement data from one selected excitation frequency can be extracted at a time. In practice this means a very time demanding task, if done manually. This process was automated by using the free, open-source program AutoHotkey. Scripts can be created with the program that for instance emulate keystrokes and mouse clicks. Essentially, the script iterates through all excitation frequencies and automatically saves the displacement data in separate text files, one for each frequency. Additionally, the script saves a separate file containing the selected measurement parameters along with a picture of the measurement set-up.

The chosen method of automation has a few limitations. Firstly, it is not completely automated since it still requires some user inputs, namely the frequency settings used for the specific measurement. The script calculates the number of iterations needed out of this data. Accordingly, if the user gives a false input, a false number of text files will be exported. Another crucial point is that the in-plane-software must be the active application when the script starts to execute. The same requirement applies during the execution of the script. If the in-plane-program loses the focus at any time to another program the export procedure will fail. It is also required that the computer has enough CPU resources to load the displacement data within the time frame of 200 ms. If the data is not loaded in time, the script will still send its keystrokes regardless.

### 7.5.2 Out-of-plane automation script

The Out-of-plane mode is mainly used for characterizing the test environment (the shaker) where the actual displacement at specific frequencies are of interest. The Out-of-plane software does offer a frequency sweep option, however, only with a relative short sweep duration. For instance, a sweep from 0-20 kHz allows a maximum sweep duration time of 320 ms. Because of the mass-spring-characteristics of the test environment, this time frame is too short to let the system reach a steady state for each frequency. Since the system always reaches a steady state during in-plane measurements it is desirable to measure the same state regarding the shaker for a more compatible comparison.

For a workaround, a script was designed that gradually increases the frequency over a longer period of time. This script lets the user input measurement parameters, much like for the in-plane software, such as start-, end- and step frequency. Contrary to the in-plane software, the Out-of-plane software provides a built in BASIC coding environment. This allows more flexibility to control the MSA and offers also the possibility to read out data directly from a file. In other words, the AutoHotkey solution can be neglected, providing a much more stable automation process.

In addition to the frequency sweep script another one was created that lets the user iterate voltage increments. This type of measurement is not provided by the PSV-software. The script is used to research voltage linearity of the testing environment. For both scripts there is also an option to, automatically, read out either the applied voltage or current for each frequency/voltage point. This measurement is carried out externally, using a Digital Multimeter (DMM) (Agilent 34401A). The voltage/current measurements are started by the BASIC script using MATLAB as a client. The result of the voltage/current measurement is saved, by the MATLAB client, in a separate data file. The external measurement can be used to either verify the selected voltage or to detect a possible saturation of the amplifier.

After a finalized measurement the script will have saved one separate file of displacement data for each voltage/frequency. Each file contains displacement data from all frequencies in the specified frequency range. Since only one frequency per file is of interest, this specific data is extracted by a MATLAB script. The script iterates all files and saves the relevant displacement data in an extra data set. This data set allocates considerably less memory and is easy to calculate and handle within MATLAB.

## 7.6 How to set up a measurement

One very important measurement set-up parameter, common for all of the modes, is to ensure that the specimen is placed as horizontally as possible. If the object is tilted, a smaller amount of light is reflected, causing a lower measuring signal. The depth of field is very slim when magnifying optically on such small focus distances. If a tilt is present, even by a few degrees, the measuring area (what the CCD camera registers) can be in focus on one side and be blurry on the other, which could lead to inaccurate results.

When performing out-of-plane measurements the optical magnification doesn't affect the accuracy of the result. It does however ease the positioning of the laser beam, both when adjusting manually (positioning reference beam) and for the automatic positioning of the software. As for in-plane measurements optical magnification is more of an important factor since the measurement is more dependent on the resolution of the camera.

The resolution of a sweep in the out-of-plane mode is the bandwidth divided in number of FFT-lines. For this study the bandwidth of 20 kHz and 6400 points (the maximum number of lines) is used, which results in a resolution of 3.125 Hz. For an accurate frequency sweep result the frequency steps should preferably be chosen so that they correspond to points that equals the frequency of the FFT lines. The FFT lines are evenly distributed as [0; 3.125; 6.25...19996.875; 20000], i. e., all multiples of 3.125 as a step size and a starting point at a FFT line will result in a accurate measurement. Using a step size that does not measure directly at the FFT lines will give a less accurate result since each point will be interpolated automatically by the PSV software.



## 8 Test environment

The behavior of freestanding microstructures can be best investigated when they are excited by a harmonic oscillation. To monitor and properly analyze the characteristic, in a certain frequency range, a well defined input is needed. That is, a test environment where the amplitude is known at every frequency of the desired frequency range. The specific test sensors are designed to operate within the range of the human ear (0.2–20 kHz). This allows to excite the structure, e. g., by a voice coil actuator, like a loud speaker membrane. The microstructures are primarily designed to register motions in an in-plane direction, which is normally defined as direction laying in the plane of the Si-chip. However, a test environment based on a voice coil actuator is, for this specific type of structures, only suitable for observing an out-of-plane motion. This is, as stated above, not the main direction of interest and, therefore, a system with an in-plane excitation is required. The chosen method is a system based on a piezo element.

### 8.1 Mechanical set-up

The basic set-up uses a holder where the Si-chip with the vibration sensor can be fixated. This holder is mounted between a spring and a piezo actuator (Figure 8.1). The whole set-up is pressed together so that the resulting counter force from the displaced spring is sufficient to hold together the three parts at all occurring accelerations. This mounting has the advantage of a nearly friction free displacement of the chip holder, yielding a more efficient system and, even more important, a less noisy in-plane motion. At relatively low voltages the piezoelectric element transforms the applied voltage almost linearly to an elongation of the piezoelectric stack.

### 8.2 Specifications of shaker

Due to the properties of the test sensors (size, mass, resonance frequency) there are several specifications that have to be fulfilled by the construction of the shaker:

- bandwidth of 15 kHz,

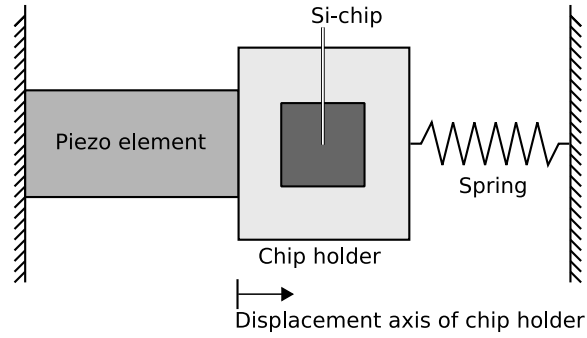


Figure 8.1: Basic set-up of shaker.

- maximum displacement amplitude of  $\pm 500$  nm,
- minimal displacement amplitude of  $\pm 5$  nm,
- uniform displacement characteristic around the equilibrium position,
- sufficient stiffness of the spring to stabilize holder and piezo element.

### 8.3 Actuator input signal

The required bandwidth is exclusively associated with the sensor properties, whereas the displacement demand is an issue of the measurement equipment. The sensor itself is designed for detecting vibration amplitudes in the order of a few nm. For in-plane measurements, however the MSA has a noise floor of 15 nm at a  $10\times$  optical magnification and assuming sample edges with ideal contrast. By choosing the maximal displacement of the shaker to a substantially larger value, the signal to noise ratio can be increased. Maximal displacement is chosen to 500 nm since the distances between the capacitive read out electrodes are designed between 1 and 5  $\mu\text{m}$ . Due to the fact that the test sensors are built to resonate within the defined bandwidth, a greater displacement amplitude of the shaker would cause the sensor to resonate at such an amplitude that contact between the free standing and the static parts would occur. This would produce distorted measuring signals and, more seriously introduce the risk of damaging the sensor.

The motion of the chip needs to be uniform around a certain position in order to get a signal that can be easily analyzed. In other words, the positive part of the sinusoidal displacement has to match the negative part, both by shape and amplitude. The post

processing stage (executed in MATLAB) of the raw data expects a pure sinusoidal signal, hence a deviation of such a signal would generate an error.

## 8.4 Piezoelectric actuator

Nowadays, there is a tremendous number of different types of piezoelectric actuators on the market. Just to mention a few: cylindrical, bending, in the shape of a disc, one actuator for positioning in all three dimensions, and so on. However, the suitable one for the shaker set-up only needs to operate in one direction. The device of choice is a multi layer actuator (P-885 supplied by Physikinstrumente). It operates by the principle of several stacked ceramic discs that are electrically insulated. The main advantage of piezoelectric stacks is the relatively low voltage required for large displacements. This is realized by connecting the individual discs of the piezoelectric stack in parallel.

All piezoelectric elements have a certain elasticity, i. e., they act like springs. The chosen type has a very high stiffness of 100 N/ $\mu\text{m}$  and can withstand extremely high external forces. When acting against an external spring load, which is the case of the shakers mechanical set-up, the actuators maximal displacement decreases, described by:

$$\Delta L_{0_{max}} = L_0 \left( \frac{k_T}{k_T + k_S} \right), \quad (43)$$

where  $L_{0_{max}}$  is the maximal displacement with external spring load,  $L_0$  is the maximal nominal displacement (nominal displacement achieved at an applied voltage of 100 V),  $k_T$  is the stiffness of the actuator and  $k_S$  is the stiffness of the external spring.

A high stiffness of the actuator in relation to the stiffness of an external spring yields a lesser loss of dynamic displacement. The main drawback of the stacked piezoelectric design is its sensitivity to tensile stress. Therefore, it is recommended by the manufacturer that a spring load should applied for offsetting the actuator to a compressed state. The recommended value is up to 50% of the maximal nominal displacement. In the realized shaker set-up this is ensured by a stiff fixation spring. The nominal displacement of the P-885 is specified to 8  $\mu\text{m}$  and a reduction with an external spring to 4  $\mu\text{m}$  still easily satisfies our initial requirement of 0.5  $\mu\text{m}$ .

The expansion of a piezoelectric resistive actuator is conducted by applying a strong electric field within the material. This polarizes the material and has the effect that when the applied electric field is polarized in the opposite direction to change state from elongation/contraction, a delay is introduced due to charge stored by the initial polarization. In other words, it is a system with hysteresis, i. e., the displacement at a specific voltage is dependent on the previous state. The impact of hysteresis, specifically on a sinusoidal driven system, results in a distorted sinusoidal motion. The width of the hysteresis depends on the applied voltage, whereas at large signal operation a maximum deviation of approximately 10–15% can be registered. For small signals, however, the deviation is typically around 2%. This behavior only occurs in an open loop system and can almost completely be compensated by regulating the voltage in a closed loop system.

The necessary time to expand the actuator from its resting state with no applied voltage to the nominal length depends inversely on the resonance frequency and can be approximated by:

$$t_r \approx \frac{1}{3f_0}, \quad (44)$$

where  $t_r$  is the rise time and  $f_0$  the resonance frequency.

The P-885 has a specified resonance frequency of 135 kHz resulting in an expansion time of 2.5  $\mu$ s which corresponds to a bandwidth of 40 kHz. This bandwidth satisfies the requested shaker bandwidth of 15 kHz. In fact, the real bandwidth of the shaker is drastically higher since only a fraction of the nominal expansion will be used.

## 8.5 Spring

The functionality of the spring is needed for two purposes. Firstly, it has to fixate the piezoelectric stack and the holder. Thereby, a spring with sufficient stiffness has to be chosen which is compliant enough not to compromise the functionality of the actuator. The maximum stiffness that is allowed from that point of view is about 10% of the actuator's stiffness. This is in our case 10 N/ $\mu\text{m}$ . The second aspect is to assist the fixation of the vibrating chip holder. When the actuator changes its state from elongation to contraction at maximal displacement the spring has to prevent the creation of a gap between actuator and holder occurs. To estimate the force (see Figure 8.2) needed for the harmonic movement the actuator's maximum acceleration at the specified maximum frequency and displacement is calculated by:

$$\hat{a}_{max} = \hat{x}(2\pi f_{max})^2, \quad (45)$$

where  $\hat{a}$  is the maximum acceleration of the actuator,  $\hat{x}$  is the maximum elongation of the actuator and  $f_{max}$  is the maximum frequency.

This generates a force of:

$$F_{max} = (m_c + m_h)\hat{a}, \quad (46)$$

where  $F_{max}$  is the maximum force acting against the spring,  $m_c$  is the mass of the Si-chip and  $m_h$  is the mass of the chip holder.

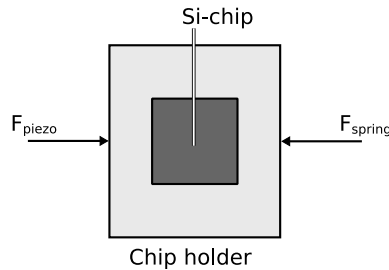


Figure 8.2: Forces applied on chip holder and Si-chip.

$F_{max}$  was calculated to 2.1 N. The actuator can fully operate at preload forces up to 50%

of the blocking force, specified to 400 N. Applying a preload force does not affect the maximum actuator displacement and the spring preload can therefore be set to far higher value to further suppress the risk of generating a gap.

To suppress disturbing vibration modes in the perpendicular plane. To minimize this effect as good as possible a short spring with a big diameter is needed. The provided spring is of plate type (Febrotec 0S4202) which has a length of 0.4 mm (unloaded) and a diameter of 8 mm. It has a stiffness of 0.17 N/ $\mu\text{m}$ , i. e., to produce the minimal specified preload force of 2.1 N the spring has to be compressed by 12.4  $\mu\text{m}$ . The spring can maximally be compressed by 200  $\mu\text{m}$  and it is chosen to be mounted with a compressed length of half of that. This maximizes the operational displacement range and ensures that no gap will originate. The resulting preload force is thereby 17 N, which is well within the maximal allowed force of 400 N.

The choice of the spring strongly affects the resonance frequency of the shaker system. It has to be ensured that the resulting resonance frequency will be outside of the operating bandwidth. The resonance frequency is calculated by:

$$f_r = \frac{1}{2\pi} \sqrt{\frac{k_s}{m_{Si} + m_{holder}}} \quad (47)$$

where  $f_r$  is resonance frequency of the shaker,  $k_s$  is the spring stiffness,  $m_{Si}$  and  $m_{holder}$  are the chip mass and holder mass respectively.

The resulting resonance frequency with the provided spring is 2.7 kHz. Therefore, a flat displacement characteristics within the specified bandwidth cannot be expected. In a next step an improved system with a stiffer spring has to be designed to improve the functionality of the shaker.

## 8.6 Electrical estimations

The function generator of the MSA has an output voltage range of  $\pm 10$  V and a current limitation of  $\pm 50$  mA. To examine whether the generator is sufficient within the operating range a few electrical estimations have to be done.

The simplest equivalent circuit of the piezo element is a capacitor:

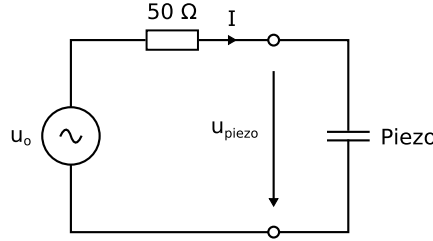


Figure 8.3: Equivalent circuit of the piezoelectric stack.

The piezo actuator (P-885) has a relatively large capacitance of  $0.6 \mu\text{F}$ . To fully expand and compress the actuator the expected charge/discharge current is therefore also large. The voltage needed to fully expand the actuator to the defined maximum displacement ( $500 \text{ nm}$ ) was calculated to  $\pm 7.8 \text{ V}$ , see (48).

$$V_{max} = V_{L_0} \frac{\Delta L_{req}}{\Delta L_{0_{max}}}, \quad (48)$$

where  $V_{max}$  is the voltage to actuate to maximal requested displacement,  $V_{L_0}$  the voltage for nominal unloaded displacement,  $L_{req}$  the requested maximal displacement and  $L_{0_{max}}$  the maximal nominal displacement with external spring load.

The estimated current is calculated to  $\pm 1.1 \text{ A}$ , using Equation (49).

$$I_{max} = 2\pi f_{req} V_{max} C_{piezo}, \quad (49)$$

where  $I_{max}$  is the peak amplitude of an alternating current to actuate to specified displacement at maximal specified frequency,  $f_{req}$  the requested maximal operation frequency,  $V_{max}$  the voltage to actuate to maximal requested displacement and  $C_{piezo}$  the capacitance value of piezo actuator.

The piezo element can also be contracted by applying a negative voltage. Up to 20% of nominal elongation is possible to accomplish. In this range the displacement has the same voltage dependence for negative as for positive displacements. Therefore, no offset voltage

is needed to drive the shaker with a sinusoidal input voltage. As already mentioned, the hysteresis increases with the applied voltage. By choosing 0 V as bias point this effect is thereby suppressed. Another advantage is that the dynamic range is maximized, in case future measurements at higher voltages than the specified one needs to be done. Consequently, the build in function generator meets the requirement of the voltage range.

However, there is a shortage of current, an additional 1.1 A is needed. The generator only supplies  $\pm 50$  mA, which is solved with a power amplifier (HP 467A).

## 8.7 Assembly of shaker

The holder has to be light in order to optimize the efficiency of the piezo actuator as well as to minimize the associated inertial force, which has an impact on the needed fixating force. To withstand the relatively high forces produced during operation, it also needs to be rigid. The material PEEK (polyetheretherketone) is therefore chosen due to its high strength-to-weight ratio. The Young's modulus is 3700 MPa and it has a density of  $1300 \text{ kg/m}^3$ . The fixating block in contact with the actuator is constructed with the same material to electrically isolate the piezoelectric stack. To adjust the prestress of the plate spring, a screw is mounted through the second fixating block (made out of aluminum). There is a small ball located on the tip of the screw to suppress possible shear forces, which the piezo stack is very sensitive to. The final assembly of the shaker, with a Si-chip mounted onto the holder, is depicted in Figure 8.4.

## 8.8 Evaluation of the test environment

To see whether the shaker gives the output it was designed for, three properties are investigated:

- shape of the motion,
- displacement characteristics,
- voltage dependence.

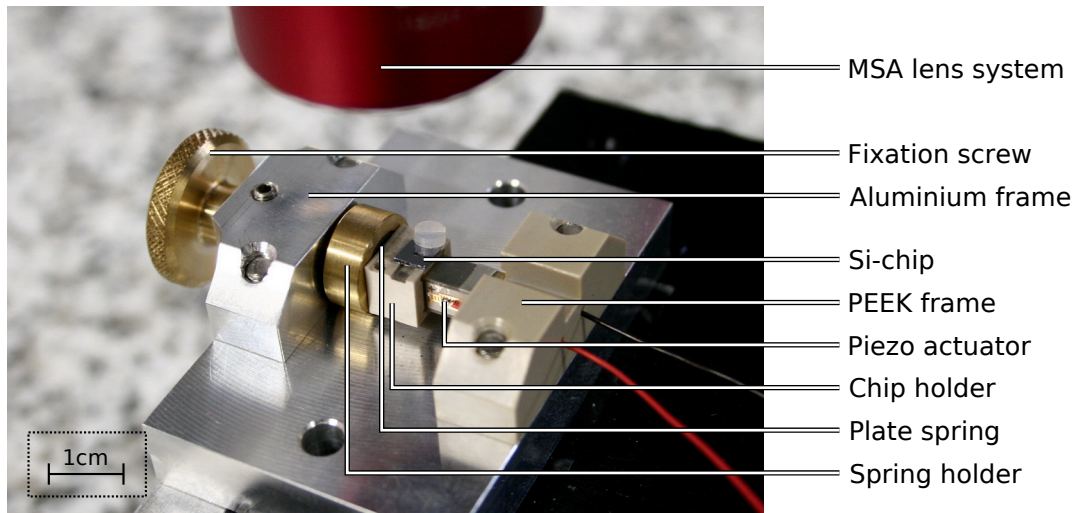


Figure 8.4: Assembly of the shaker for Si based accelerator sensors.

### 8.8.1 Harmonic motion

The confirmation of a harmonic oscillation behavior is conducted by an in-plane measurement in the PMA-mode of the MSA. The measurement is performed at maximal specified voltage (7.8 V) since the hysteresis is at its most for high voltages. Figure 8.5 shows the result of such a measurement. For comparison, a sinusoidal is overlaid. The measured values clearly follow the sinus curve, however, the measurement is fairly noisy due to the rough surface of the Si-chip holder, hampering the pattern recognition of the software. The noise level is approximately twice as high as the specified noise floor. The hysteresis is small enough to cause only a displacement deviation below the noise floor for in-plane measurements and can therefore be neglected. This signal level will be used exclusively for characterizing the shaker. The sensor measurements will be conducted at distinctively smaller input voltages which lead to even smaller hysteresis levels.

### 8.8.2 Out-of-plane measurement set-up

When a sensor is characterized using the shaker, the sensor has to be placed in an in-plane position. However, when the shaker itself is characterized no sensor is required. The additional free space allows measurements in the out-of-plane mode of the MSA (PSV-mode). The main advantages of the PSV mode over the PMA-mode are twofold, namely measurement time and accuracy. During measurement of the piezoelectric element, the

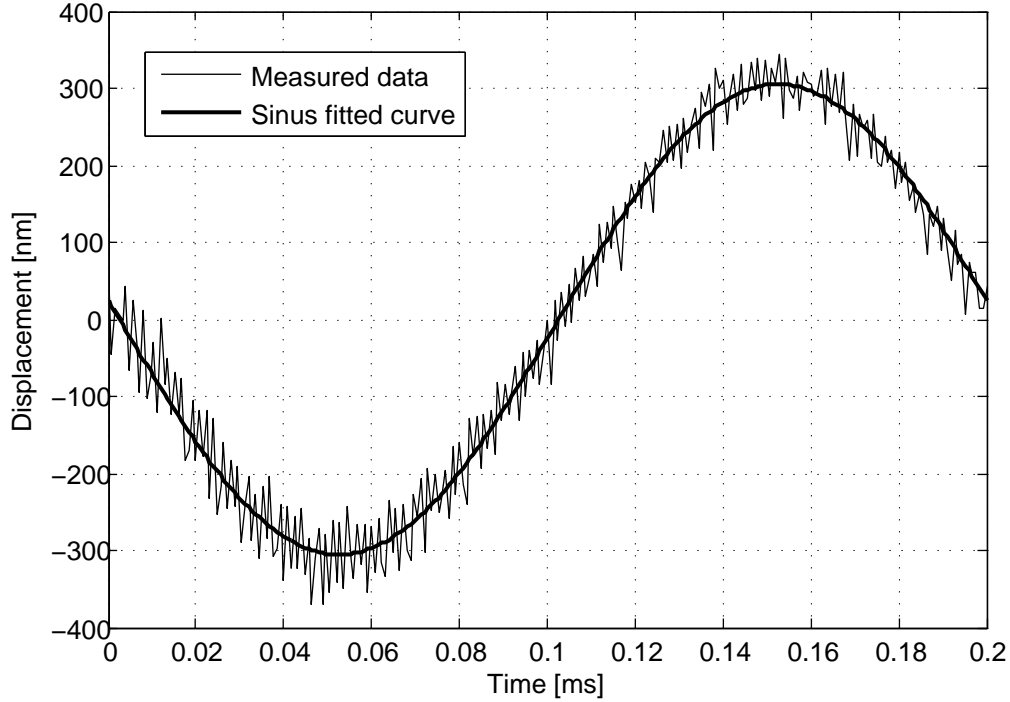


Figure 8.5: Harmonic displacement of the holder at 5 kHz and  $\hat{u} = 7.8$  V.

current through it is also measured separately and registered for each corresponding voltage value. This is conducted via the GPIB interface of a Digital Multimeter (DMM) (Agilent 34401A). By this procedure, it is ensured that the shaker is provided with sufficient current throughout the whole measurement range and also if it shows a linear current increment. The shaker is characterized with the out-of-plane measuring mode, hence, the shaker is placed vertically. The measurement is performed on the edge of the Si-chip holder (see Figure 8.6) to register the motion. Since the shaker, in this set-up, is placed perpendicular to the normal orientation an additional force is introduced, namely the gravitational force on the holder. However, the impact on the displacement amplitude can be neglected. The only effect is that the spring is slightly compressed, resulting in a higher preload force which will lead to a higher operational current. The change in preload force in terms of percentage is calculated to be 0.1 %, which can be seen as an insignificant current change for this application.

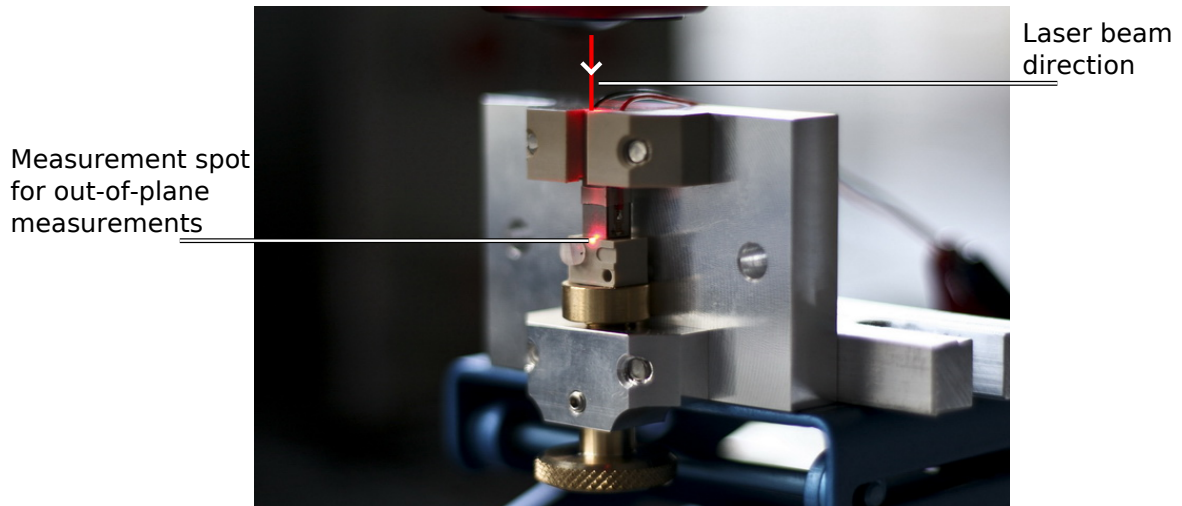


Figure 8.6: Shaker mounted for out-of-plane measurement.

### 8.8.3 The shakers frequency dependence

The shaker is designed to give a flat frequency dependence up to 15 kHz, however, according to the spring calculations in Section 8.5 the provided spring will cause a resonance of the system somewhere around 2.7 kHz. A displacement peak is therefore expected at this frequency and a damping of the displacement amplitude for higher frequencies. The frequency characteristics at an applied voltage of 7.8 V is presented in Figure 8.7. The frequency resolution of this measurement is 6.25 Hz and the system is excited for 0.64 s, at every frequency point, before the amplitude is sampled to ensure a steady state.

Three interesting observations of the shaker's characteristic is found in fig. 8.7:

- position of resonance frequency,
- multiple resonance peaks,
- amplitude at low frequencies.

The resonance peak originated by the shakers internal spring-mass system was calculated to appear near 3 kHz (see Equation (47)), yet the real system resonates at 8.9 kHz. There is a considerable deviation of factor three compared to the calculations, however, it is beneficial for the shakers characteristic. When excluding the other amplitude peaks

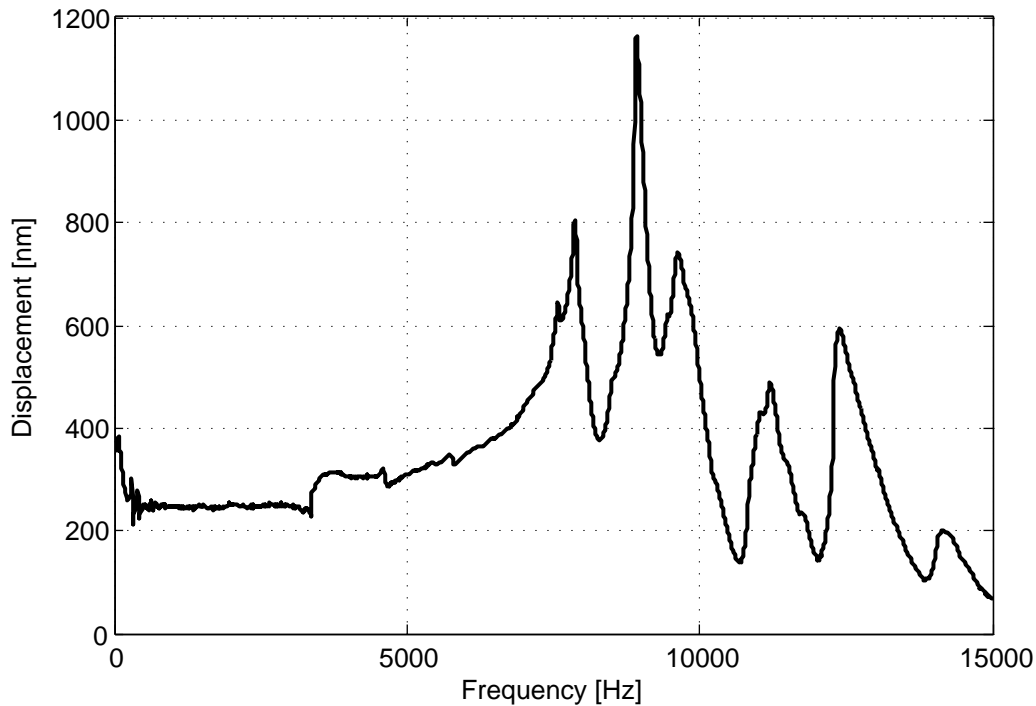


Figure 8.7: Displacement of holder at 7.8 V, measured on the edge of the holder in out-of-plane mode.

around 8.9 kHz the expected characteristics of a peak with a damping of the whole system emerges, indicating that the spring causes this specific peak.

The amplitude in the flat region was estimated to 500 nm, in reality the shaker only accomplishes a displacement of 250 nm. One solution to this would be to double the input voltage, this would however saturate the power amplifier and, thereby, require another hardware. A displacement of 250 nm is in fact sufficient to perform relatively good measurements in the PMA-mode, therefore, the lack of displacement amplitude is not considered as a main issue to be solved.

The multiple resonance peaks can be derived as a material effect. Since the piezoelectric stack develops large forces, relative to the resulting displacements, the compression of the different parts of the system has to be taken into account in the model of the shaker. A more sophisticated model than the one in Figure 8.1 is presented in Figure 8.8, where the dashed springs represent the compression of the various materials used in the shaker system.

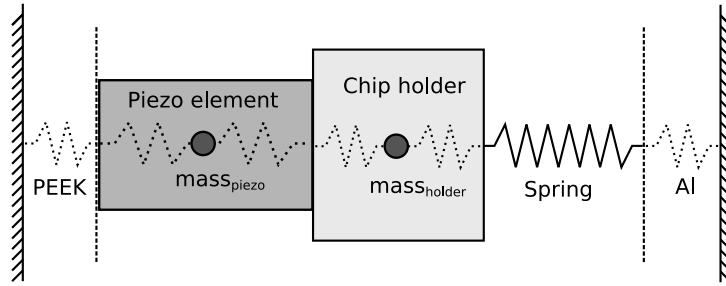


Figure 8.8: Enhanced spring–mass–system model of shaker.

Each of these components has the ability to resonate and, thereby, causing an unwanted displacement of the holder. To confirm the source of this interference, a measurement on the PEEK frame just above the piezoelectric stack was conducted (also as an out-of-plane measurement see Figure 8.6). The results are presented in Figure 8.9, where the measurement is conducted at 3.9 V. A better representation of the compression characteristics would be at 7.8 V. Unfortunately, the shaker was disassembled after these measurements and after reassembling the shaker the resonance characteristics were strongly shifted due to a different preload. The fixating screw is not accurate enough to reproduce identical conditions.

Anyhow, a few important conclusions can be drawn from the results. Firstly, the PEEK-material is hardly affected by the displacement of the holder up to approximately 7 kHz. After that the peak amplitudes are considerably large, compared to the displacement of the holder. Especially for peak number one, five and six, implying that these peaks are mainly caused by the PEEK frame. Whereas peak number two is caused by the spring plus holder mass system, with the assumption that the spring is softer than the material, i. e., has a lower spring constant, and thus the highest resonance amplitude. The remaining two peaks (number three and four) are assumed to originate from the holder. This can however not be verified by a measurement due to the set-up of the shaker. To fully analyze the shaker system, the compression at every surface contact point has to be measured.

Note that the displacement characteristics in Figure 8.9 is on the opposite side of the contact area between PEEK and the piezoelectric stack. The actual compression amplitude is ever larger since only a scaled displacement can be registered on top of the PEEK frame. The same type of measurement was made on the opposite side of the shaker, that is on top of the fixating screw, where a similar pattern appeared only with approximately

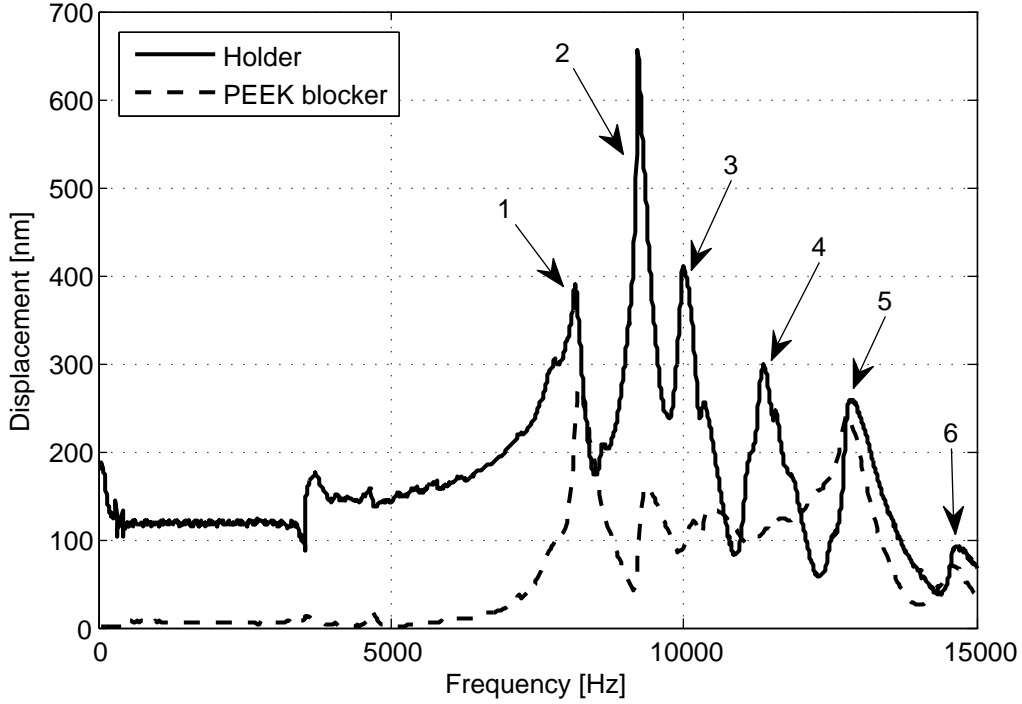


Figure 8.9: Displacement of holder and PEEK frame at 3.9 V.

half the amplitudes. This due to the fact that aluminum is stiffer than PEEK and is therefore not as easily compressed.

One additional effect, which is not illustrated in Figure 8.8, occurs during excitation of the shaker, namely, that both frame elements are not only compressed but also experiences bending, introducing an additional spring effect.

The piezo stack is specified to elongate 500 nm at 7.8 V [15], yet a displacement of 1150 nm was registered. This raises the question whether the spring manages to extend enough or that a air gap arises. The produced force of the actuator in dynamic operation can be calculated by:

$$F_{dyn} = 4\pi^2 \left( \frac{\Delta L}{2} \right) f^2, \quad (50)$$

where  $F_{dyn}$  is the force generated in dynamic operation,  $\Delta L$  the displacement of piezo and  $f$  the operating frequency. This results in a force of 1.1 N (at 15 kHz), the preload

force of the spring is 17 N and is thereby high enough to prevent a gap.

#### 8.8.4 Voltage dependence

The shaker was measured in a frequency range of 1–15 kHz at every 1 kHz. At each frequency point the displacement was measured at an applied voltage between 0–10 V at every 0.1 V. Figure 8.11 shows the characteristics for excitation frequencies of 1–7 kHz. For frequencies between 1 and 4 kHz the shaker behaves as expected, where a relative voltage increment causes a proportional displacement increment. However, for frequencies of 5–7 kHz the shaker starts to resonate. The piezoelectric actuator still elongates correctly to applied voltage but since the system resonates the same voltage-to-displacement ratio does not apply anymore. Therefore, for comparing resonance amplitudes of sensor structures at different applied voltages over 4 kHz another scaling has to be used.

The power amplifier delivers a correct linear current level with a harmonic waveform, thus, the piezoelectric actuator too actuates linearly to applied voltages. In a simple spring-mass system the resonance amplitude is theoretically proportional to the excitation amplitude. The component causing the shaker system to resonate is the compression of the PEEK material. This compression emulates a non linear spring. The result of this can be seen for frequencies above 7 kHz, where the shaker starts to resonate (Figure 8.10).

Since the system has a non linear voltage dependence this also affects the resonance frequencies. In Figure 8.12 two measurements are presented with an applied voltage of 1 and 10 V. This voltage difference cause the shaker system to shift its frequency characteristics by approximately 0.5 kHz. The two curves have been normalized to give a better overview of the frequency shift.

When measuring the displacement for frequencies at or close to a resonance peak, it was found that the displacement characteristics are matched to the previous non linear shape up to a certain level, depending on the resonance peak. Over this level, however, the displacement saturates. The displacement at the two highest resonance peaks can be seen in Figure 8.13. Possible explanations for the saturation of the system are:

- the shaker is physically blocked by the fixating part,
- insufficient power,

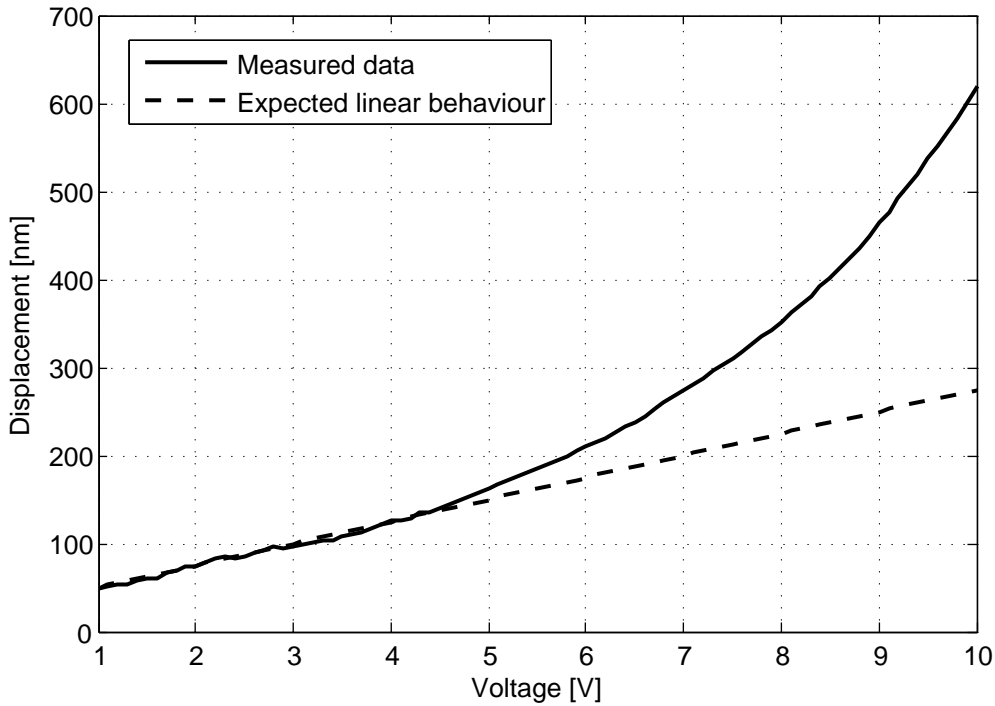


Figure 8.10: Displacement of holder at 15 kHz.

- saturated material deformations.

If the shaker is assembled correctly, a displacement margin of approximately  $\pm 25 \mu\text{m}$ , restricted by the spring should be left. This leaves a margin with a factor of approximately 25, which should be large enough to exclude the possibility of a physical contact. Another fact that supports this presumption is that the saturation occurs at different displacements. The issue of insufficient power, as already been mentioned, has been measured and exhibited no saturation. It appears as if the compression of the PEEK-material reaches a certain point where it stops acting like a spring and become substantially stiffer beyond this threshold, and therefore, saturating the displacement at resonance. This raises the question of how different displacements can appear at the saturation point. The shaker system consist of three parts that all act like springs and are made out of PEEK. Each of these "springs" contribute to the resonance characteristics and can independently produce interference, which could support the arise of different saturation amplitudes.

To be able to easily compare two measurements at different voltages this behavior could

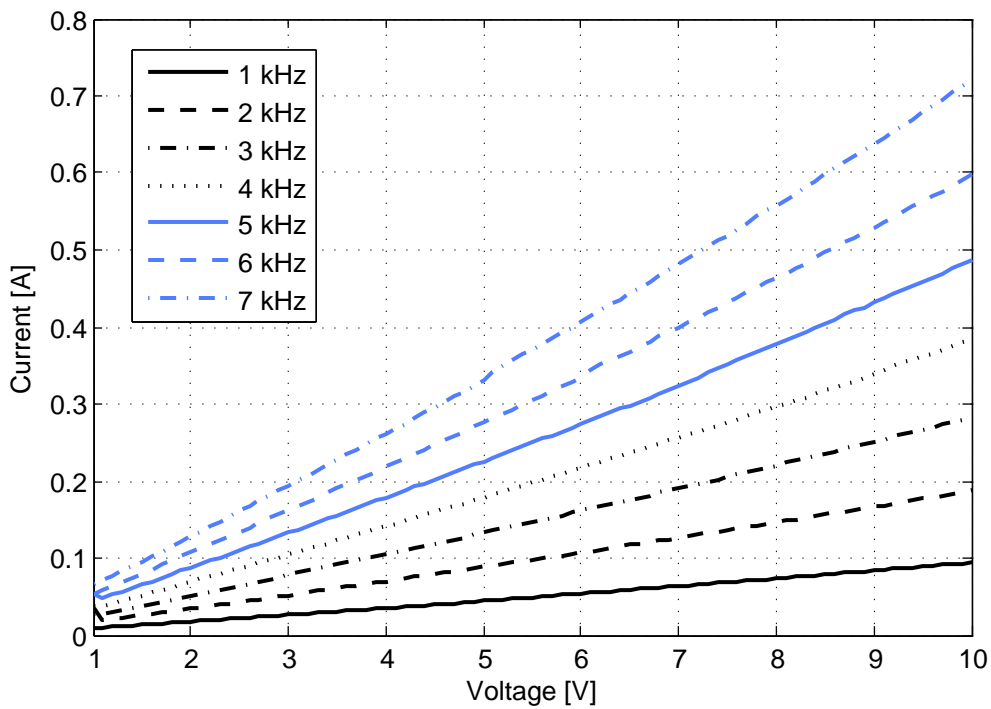
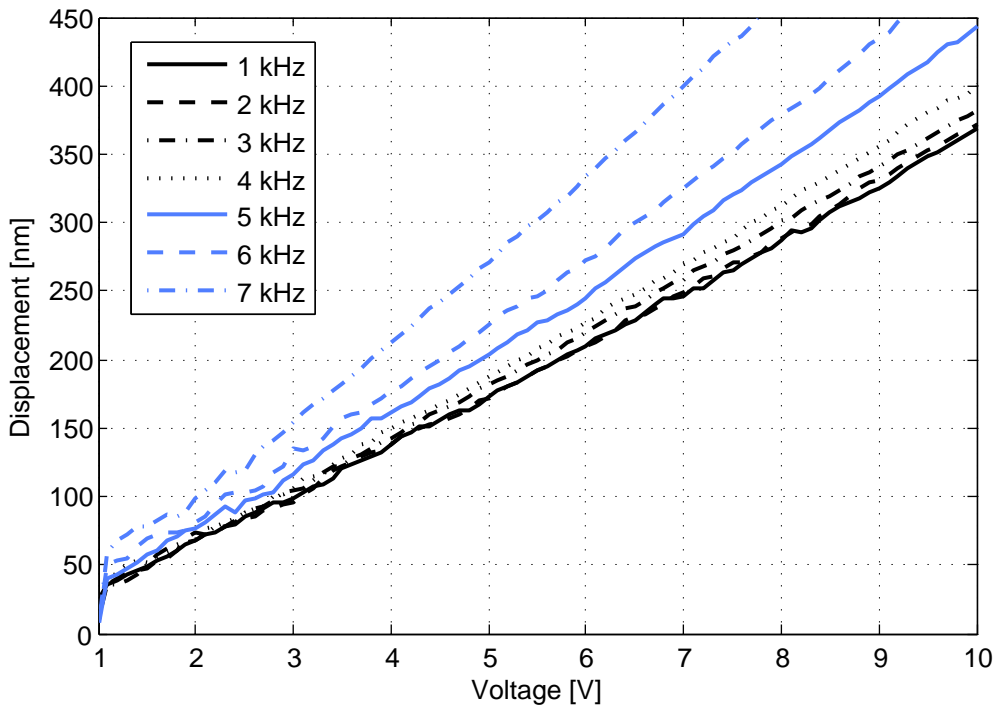


Figure 8.11: Displacement and drive current of shaker.

be linearized. However, the complexity of the voltage dependence over 7 kHz makes it

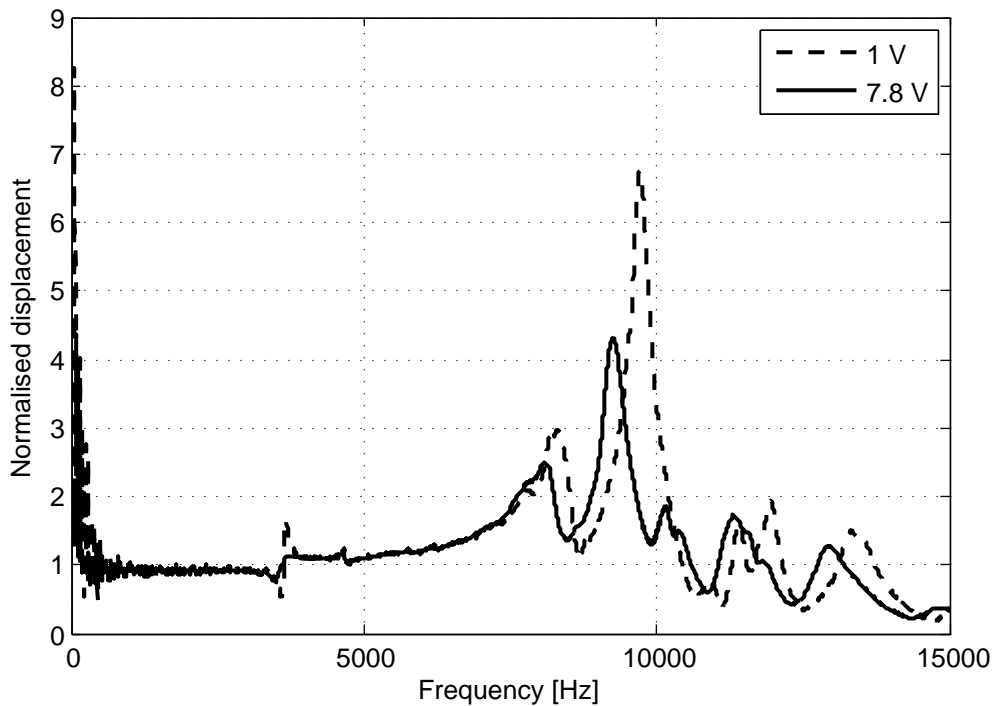


Figure 8.12: Frequency characteristics of shaker at 1 and 7.8 V.

difficult to form a precise scaling model for comparing sampled sensor results at different excitation levels. A good example showing the complexity of modeling the system can be seen in Figure 8.14, where a 4th degree dependence (result from a basic fitting function) followed by a saturation is measured.

The practical solution, because of the complexity, can be solved by manually mapping the voltage dependence of the shaker for each frequency. This solution is, however, very time consuming because of the amount of measurement data needed to make an accurate linearization. This adjustment, however, only needs to be done if frequencies over the, already, linear region of the shaker are of interest.

## 8.9 Possible improvements of the shaker

The first and most obvious improvement is to change the spring to a stiffer one that will produce a resonance frequency distinctively well above 15 kHz. A stiffer spring will reduce the overall displacement magnitude. For example, a spring that is four times as stiff as

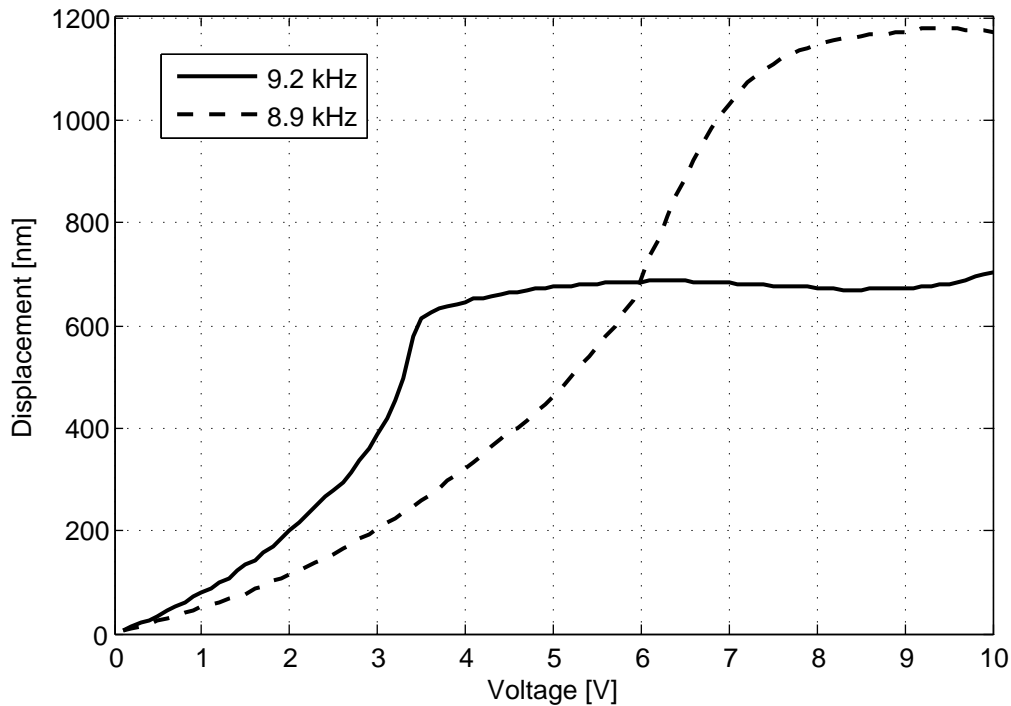


Figure 8.13: Displacement of shaker at 9.2 and 8.9 kHz.

the currently used one, reduces the displacement only by 0.5% (see Equation (43)), which can be considered as an acceptable reduction.

Replacing the PEEK frame by a stiffer material will also produce a better frequency characteristic. Modifying the frames to be thicker would also improve performance, mainly by reducing the bending effect.

A material change of the holder would also be preferable, however this would increase the weight. For instance a change to aluminum would double the weight and thereby degrade the functionality of the actuator at high frequencies.

Since the system experiences relatively large forces and considerably large compressive stresses, at such small displacements, a material compression is inevitable. A good solution to this problem would be to construct a user defined input signal based on the frequency characteristics of the shaker in order to produce a flat frequency response throughout the whole specified bandwidth. At this point, the feature of defining special input signals is not provided in the in-plane measuring mode (however, in out-of-plane mode). Future

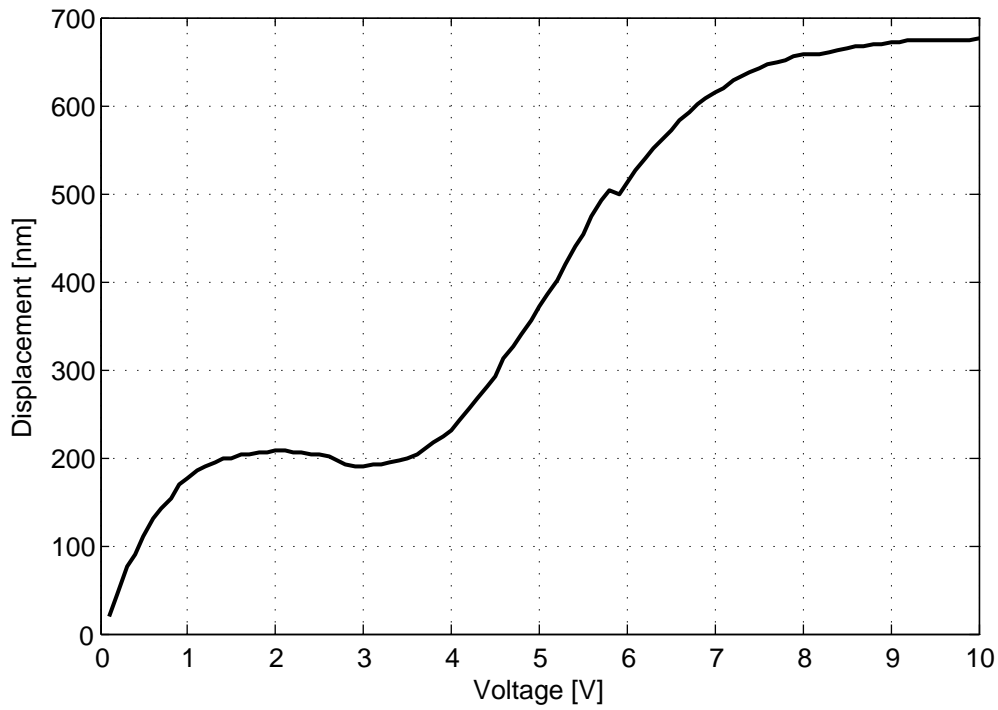


Figure 8.14: Displacement of shaker at 10 kHz.

versions of the software will include the ability control the in-plane measurements by a built in macro function which would enable the possibility to operate the integrated generator.

## 9 Work flow for vibration sensor characterization

This section of the thesis will explain the different approaches on how to perform a successful characterization of a vibration sensor. Each approach has its advantages and disadvantages regarding speed, accuracy and disk space.

The first method is the most straight forward one, which is to make a complete scan using the PMA-mode (in-plane). In order to register the resonance peak, as well as its width, the frequency steps must be relatively small, steps of 10 Hz can be considered a sufficient resolution. The small step size is more crucial for sensors where the resonance peak is situated at higher frequencies since the width of the peak is automatically thinner. This method has the advantage of a measurement where the whole frequency range is represented at a high resolution. The disadvantage is the time needed for such a measurement. The amount of time also depends on the number of measuring points for each separate frequency step, but even when using few points the measurement typically takes several of hours. Given the long operation time and the fact that the sensor mass is vibrating, there is a risk of dislocating the sensor during a measurement. Even if the dislocation is only a few  $\mu\text{m}$ , the measurement could be voided and, thus, wasting several hours of measurement data.

The second method is similar to the first one, but instead of making a measurement with a high resolution, one starts with larger frequency steps. For instance, steps of 200 Hz might be a good starting point. This would mean a time reduction with a factor of 20 compared to the measurement with 10 Hz steps. Once a suspected resonance peak is located, another measurement around this frequency is conducted with a smaller step frequency. This method does not always work flawlessly, it can sometimes be hard to immediately detect a resonance peak. There are occurrences where there are several candidates of where the resonance peak might be. Even so, after measuring with a high resolution around all candidates, the time and disk space consumed is considerably less than for a complete scan (method one). This method still offers the same resolution around the point of interest with a lesser risk of the sample being dislocated. Also, there is the possibility to stitch together multiple measurements of one sensor to get a representation over the whole frequency range.

The third method used a combination of PSV (out-of-plane) and PMA (in-plane) measurements. It was found that when resonating of the sensor occurs, not only does in-plane

displacement increase but also out-of-plane displacements. In fact, the sensor mass starts to oscillate in a wave like manner. These oscillations are extremely small but can be detected since the PSV-mode is so accurate. Taking advantage of this phenomenon, a quick frequency sweep (0-20 kHz) can reveal the resonance frequency within seconds. Since the PSV measurement is in the "wrong" direction it is followed by a high resolution PMA measurement around the found resonance frequency. This method works very well for frequencies over approximately 2 kHz. For lower frequencies the sensor plate does not resonate rigorously enough detect out-of-plane resonance.

## 10 Results

### 10.1 Optical evaluation

An optical microscope was used to measure the relevant dimensions of the test sensor. The microscope system includes a digital camera head along with an image software that enables the user to make on-screen dimensional measurements. Magnifications of 10x, 20x, 50x and 100x are available and the camera head resolution is 1 Megapixel, which is adequate for characterizing the test sensors.

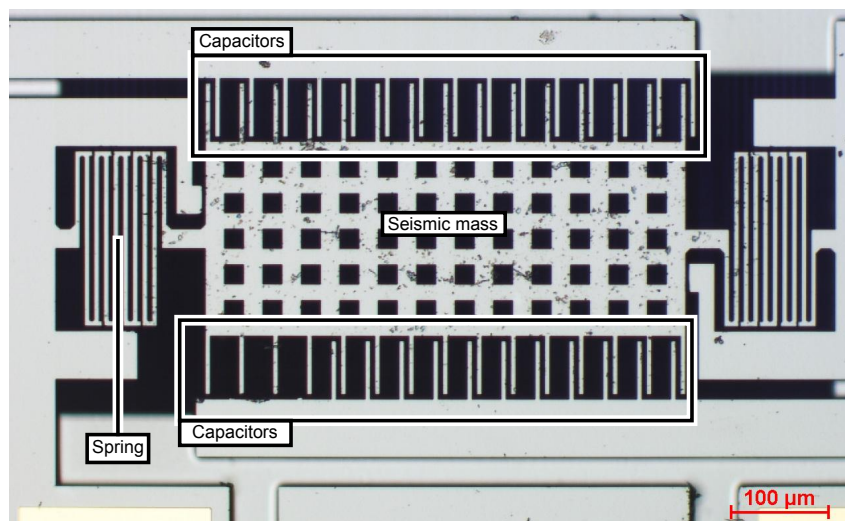


Figure 10.1: Microscopic overview of a vibration sensor.

Figure 10.1 depicts one of the produced test sensors. The picture was taken at a magnification of 10x which gives an overview of the whole seismic mass and the springs. From this view we can conclude that the manufacturing of the vibration sensor was a success, at least in terms of stiction. None of the beams or the spring elements are in contact with each other and the movable elements seems to be free-standing. Notable is also that four of the beams are broken off, most likely during the rinsing process. The unwanted black spots that can be seen on both the frame and the mass are leftover coating residues. This particular sensor is especially contaminated, but most of the other sensors were far cleaner.

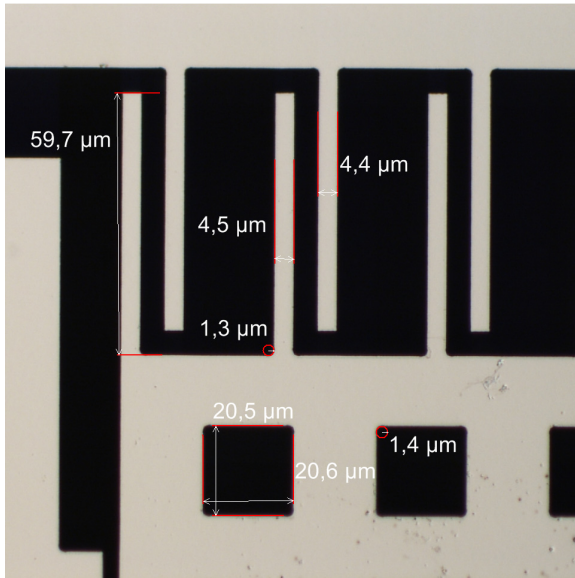


Figure 10.2: Micrograph of the top side of a test sensor.

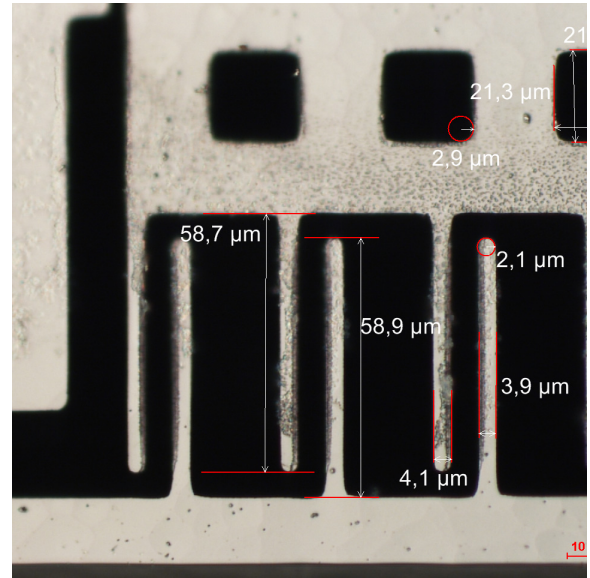


Figure 10.3: Micrograph of the backside of a test sensor.

Figure 10.2 and 10.3 depict dimension measurements of a beam section from the same sensor as in Figure 10.1. Both pictures depict the same pair of beams but from opposite sides. In the top view of the sensor the structure is almost as designed. The contours match the mask that were used and all edges look sharp. The dimensions, however, do not match perfectly. For instance the beam width, for this sensor, was designed to be 5 μm and the measurements show that the result is about 0.5 μm smaller. Overall, both plate and spring dimensions are slightly smaller. The surface on the opposite side of the sensor (see Figure 10.3) is rougher due to the wet etching. It also shows that the corners are not as sharp and the beams are not as straight as on the top side. This is due to the deep plasma etching process (20 μm deep). It is particularly difficult to get a good result in narrow trenches, like between the beams. Other areas led to better results, for example the frame outline.

Figure 10.4 presents a sensor with very long and thin spring elements. They were designed to have a width of 2 μm and, as can be seen in Figure 10.5, on the rear side of the sensor the width has been reduced to only 1 μm. This is one of the more extreme cases where the slant from the plasma etch is not negligible. But, this spring also demonstrates the incredible mechanical strength of silicone.

Conclusively, from a optical point of view, the production was successful with some minor setbacks. The smaller dimensions will result in both weaker springs and lighter plate

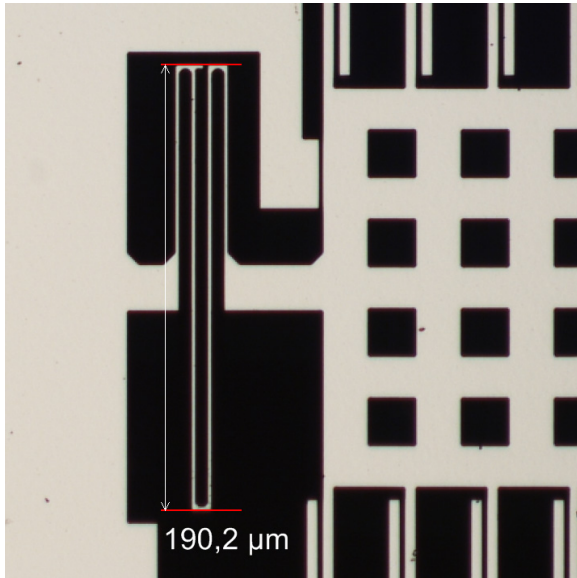


Figure 10.4: Micrograph of the top side of a test sensor.

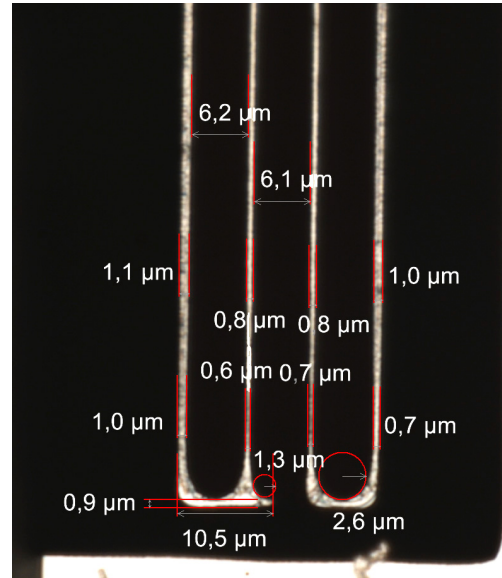


Figure 10.5: Microscopic picture of the backside of a test sensor.

masses than designed. The springs will be more affected since a larger proportion of the material will be reduced than for the seismic mass. This results in a lower resonance frequency than designed.

During the optical evaluation of a test sensor it was found that stiction between the individual walls of the spring can occur. The particular sensor in Figure 10.6 and 10.7 was designed with long spring beams, making each segment more elastic and, as a result, more prone to stiction. Stiction between two objects can arise during the production, most commonly during a "wet" process, when two surfaces come in contact and the capillary force is large enough to adhere the two.

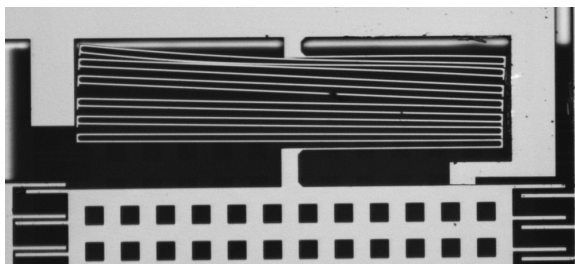


Figure 10.6: Micrograph that depicts stiction between spring beams.

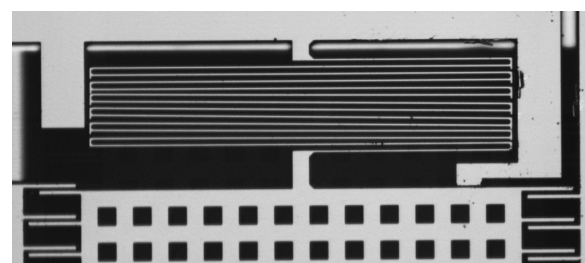


Figure 10.7: Micrograph of correctly separated spring beams.

As an attempt to reverse the stiction state, the test sensor was excited rigorously using the shaker. Figure 10.6 and 10.7 depicts the sensor before and after the shaking which shows a successful and complete separation of the spring beams. The spring stiction fault was only found on one of the test sensors.

The sensor in Figure 10.8 has an unusually large seismic mass in combination with wide and long springs. This enables large displacements, not only in the intended sensing direction but also in the direction of the other axes. This can cause the seismic mass to be dislocated under/over other parts of the chip, which occurred during an attempt to release spring stiction. Because of the unusual high forces the seismic mass got displaced by 20  $\mu\text{m}$  in the out-of-plane direction and was squeezed under the frame of the sensor. The sensor was restored to its initial state by further excitation without any notable damage.

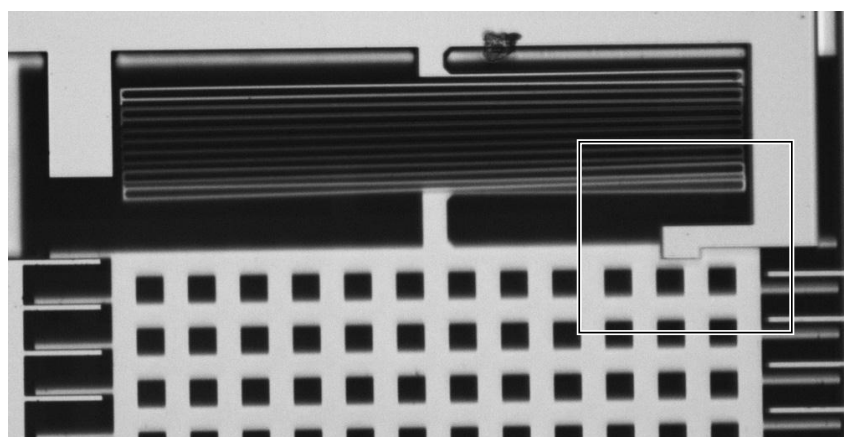


Figure 10.8: Micrograph of a vibration sensor where the seismic mass is dislocated under the frame of the sensor.

## 10.2 Frequency dependence

Measuring the frequency dependence of test sensors using a small frequency step size and a large bandwidth is, like described in Chapter 7.4, very time consuming. However, to get a good understanding how a sensor responds throughout the whole frequency range there is no substitute method. Therefore, a small number of test sensors was measured this way and Figure 10.9 presents a typical result of such a measurement .

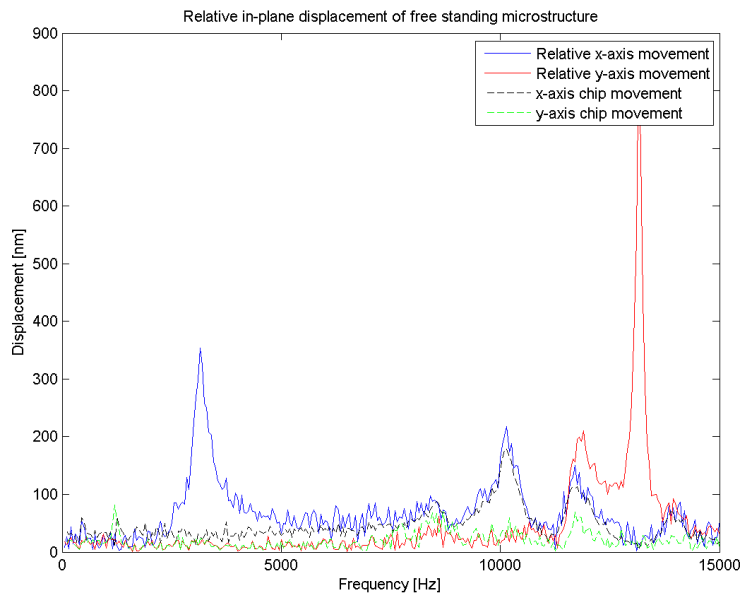


Figure 10.9: Frequency response of a vibration sensor.

The measurement was conducted with a frequency step size of 50 Hz. The sensor chip is excited in the  $x$ -axis direction. At around 3 kHz the sensor is clearly resonating in this axis. At this frequency, the chip frame is oscillating with an amplitude of around 50 nm whereas the seismic mass oscillates with almost 400 nm. It should be noted that the relative displacement movement indicates the seismic mass movement in respect to the sensor frame, i. e., displacement amplitude of the seismic mass subtracted by the amplitude of the chip. There are also a number of additional peaks in the  $x$ -axis direction. These peaks do not derive from sensor resonance (since chip and seismic mass displacements have the same magnitude) but rather from the nonlinear frequency characteristic of the shaker (see Chapter 8.8.3).

Although the sensor is excited in the  $x$ -axis direction there is a resonance peak in the perpendicular direction ( $y$ -axis) at about 13 kHz. This can occur for two reasons. Firstly, the shaker is not a perfect model of a one directional actuator, which can be confirmed by observing the  $y$ -axis chip movement in Figure 10.9. Secondly, the springs are not only elastic in the operational direction but also perpendicular to it. This creates yet another spring-mass system that also has the ability to resonate. This phenomenon would have a very small impact of the output signal if the sensor is operated and measured capacitively because the ( $x$ -axis) distance between the combs is the dominant factor. It should, however, be taken into consideration in the design of future sensors for accuracy

and stability reasons.

Most of the test sensors were characterized with the more time efficient method of making an out-of-plane measurement to get an indication where the resonance frequency could be. This is followed by a detailed in-plane measurement around that point (method explained in Chapter 9). Figure 10.10 depicts a successful result of such an in-plane measurement.

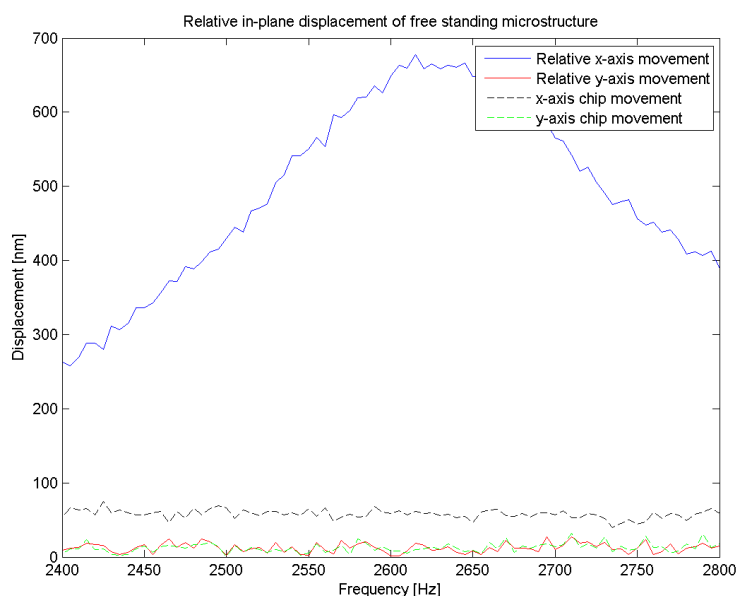


Figure 10.10: Frequency response around a resonance peak with a resolution of 5 Hz.

This measurement reveals that the sensor resonates, and also that the shape of the resonance peak corresponds to the theoretical one, see Figure 4.9.

As described in Chapter 7.2, each frequency step in a measurement is recorded by a series of pictures to determine displacements. Figures 10.11 to 10.14 show (cropped) snapshots that visualize the displacement of the actual sensor plate at the two described resonance peaks respectively.

By comparing the gaps between the combs in Figure 10.11 and 10.12 a noticeable difference can be seen. This gap difference is approximately 800 nm which corresponds to an amplitude of 400 nm, as presented in Figure 10.9.

Figure 10.13 and 10.14 shows the displacement at the extreme points in the  $y$ -axis. It is

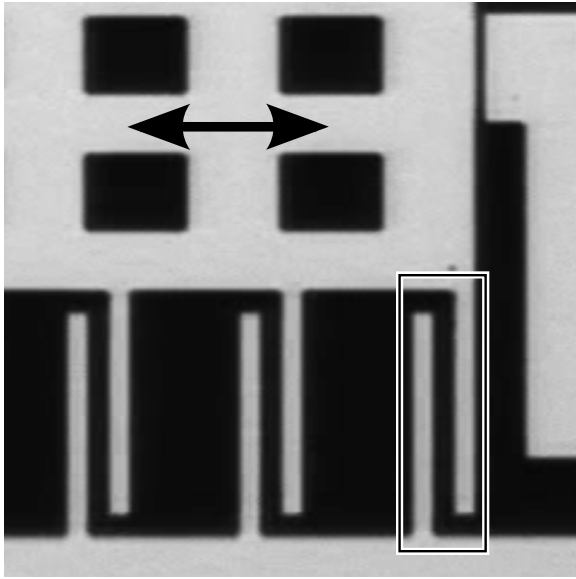


Figure 10.11: Maximum positive  $x$ -axis displacement at 3.15 kHz.

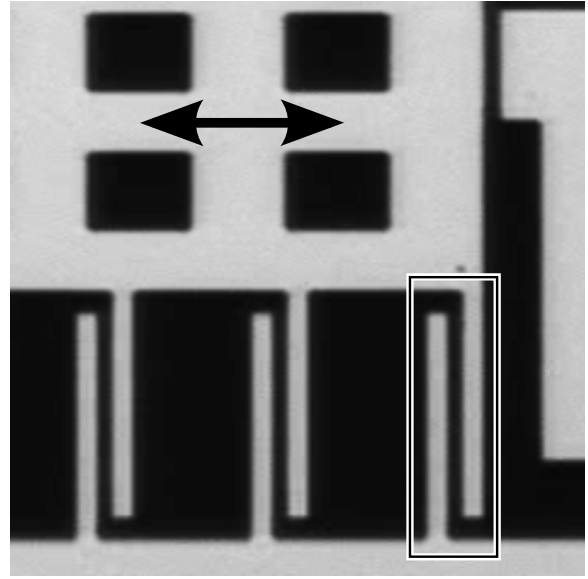


Figure 10.12: Maximum negative  $x$ -axis displacement at 3.15 kHz.

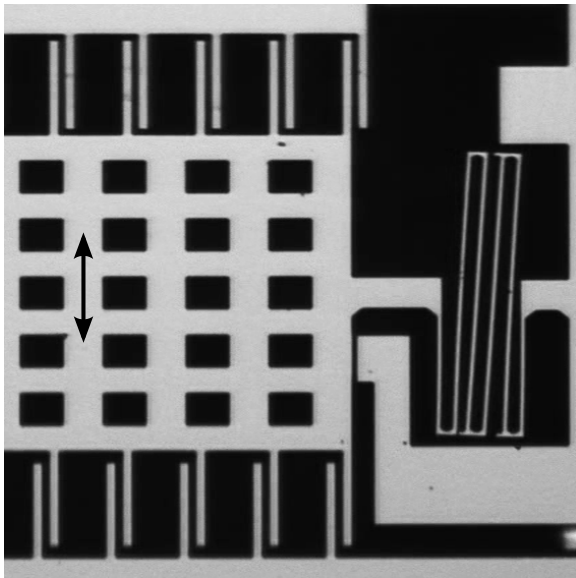


Figure 10.13: Maximum displacement in positive  $y$ -direction.

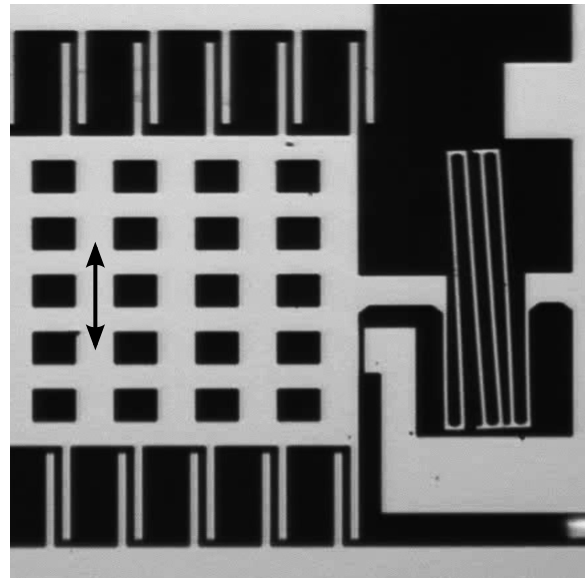


Figure 10.14: Maximum displacement in negative  $y$ -direction.

also very interesting to observe the state of the springs in both pictures. This again stresses the strength and flexibility of silicone. Also note that the spring stoppers successfully restrain the spring walls from touching.

### 10.3 Correlation of analytical and measured frequency dependence

To investigate the frequency dependence of the vibration sensors more closely we can look at sensor number 19-12. The springs of this particular sensor have two short and four long beam segments (see Chapter 5.1.2). The spring beam width is  $3\ \mu\text{m}$  and the seismic mass is  $9.79 \cdot 10^{-10}\ \text{kg}$ . The measurement with the MSA shows a resonance peak at 3.16 kHz. The theoretical resonance frequency, using the data above, is calculated to 3.67 kHz which is considerably higher than the operational resonance frequency. However, the examined actual spring dimensions in Figure 10.15 are  $2.7\ \mu\text{m}$  wide, in contrast to the designed  $3\ \mu\text{m}$ . When recalculating the resonance frequency, using this data, the result is 3.21 kHz which is very close to the measured value. Note that the small decrease in mass, due to a smaller seismic mass plate than designed, is discarded in this calculation.

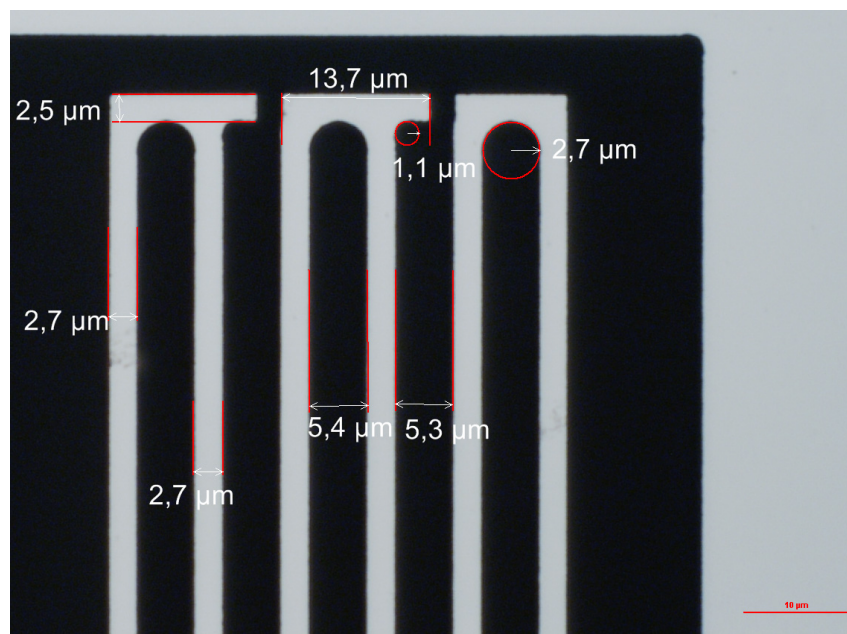


Figure 10.15: Micrograph of one of the springs of a test sensor.

The matching resonance frequencies confirms that the theoretical and the measured sensor characteristics fit well. To achieve a more accurate designed resonance frequency the dimension mismatch has to be taken in account for.

## References

- [1] James J. Allen. *Micro Electro Mechanical System Design*. CRC Press, 2005. p. 4.
- [2] Nicolo Savalli Salvatore Baglio, Salvatore Castorina. *Scaling Issues and Design of MEMS*. John Wiley & Sons, 2008. pp. 15.
- [3] Oliver Paul Jan Korvink. *MEMS: A Practical Guide of Design, Analysis, and Applications*. Springer Science & Business Media, 2010. p. 805.
- [4] Mohamed Gad el Hak. *MEMS: Design and Fabrication*. CRC Press, Taylor & Francis, 2005. p. 3-4.
- [5] Hoon Sohn Ming L. Wang, Jerome P. Lynch. *Sensor Technologies for Civil Infrastructures: Sensing Hardware and Data Collection Methods for Performance Assessment*. Elsevier, 2014. p. 280.
- [6] Yasutoshi Suzuki Jiri Marek, Hans-Peter Trah. *Sensors for Automotive Applications, Volume 4*. John Wiley & Sons, 2006. p. 269.
- [7] Min hang Bao. *Micro Mechanical Transducers: Pressure Sensors, Accelerometers and Gyroscopes, Volume 8 of Handbook of Sensors and Actuators*. Elsevier, 2000. p. 13.
- [8] Marco Carminati. *ZeptoFarad capacitance detection with a miniaturized CMOS current front-end for nanoscale sensors*. Elsevier, 2011. p. 120.
- [9] Gabriel M. Rebeiz. *RF MEMS: Theory, Design, and Technology*. John Wiley & Sons, 2004. p. 33.
- [10] Pinyen Lin Reza Ghodssi. *MEMS Materials and Processes Handbook, Volume 1 of MEMS Reference Shelf*. Springer Science & Business Media, 2011. p. 421.
- [11] Markku Tilli Veikko Lindroos, Sami Franssila. *Handbook of Silicon Based MEMS Materials and Technologies*. Elsevier, 2009. p. 340.
- [12] H. V. Jansen M. Elwenspoek. *Silicon Micromachining*. Cambridge University Press, 1998. p. 11.
- [13] Victor Chen. *The Micro-Doppler Effect in Radar*. Artech House, 2011. p. 14.
- [14] P. Hariharan. *Optical Interferometry, Second Edition*. Academic Press, 2003. pp. 143.
- [15] Physik Instrumente (PI) GmbH und Co. Picma stack multilayer piezo actuators. [http://www.physikinstrumente.com/download/PI\\_Datasheet\\_P-882\\_-\\_P-888\\_20150123.pdf](http://www.physikinstrumente.com/download/PI_Datasheet_P-882_-_P-888_20150123.pdf), 2015. p. 1.

# List of Figures

3.1	Schematic of the very first cantilever structure prototype for acceleration sensing . . . . .	3
3.2	Schematic of the cross section of a bulk machined accelerometer with over-load protection and air damping. . . . .	4
3.3	Schematic of the cross section of a bulk machined capacitive accelerometer. . . . .	5
3.4	Surface micro machined capacitive accelerometer. . . . .	6
4.1	Spring-mass-system where the mass is displaced by the distance $x_0$ along the axis. . . . .	7
4.2	Model of a damped spring-mass-system and the acting forces . . . . .	9
4.3	Model of a forced damped spring-mass-system, excited by a sinusoidal force. . . . .	13
4.4	Two examples of the homogeneous and the particular solution added together. . . . .	15
4.5	Transfer function of a damped spring-mass-system, where the mass is excited with a harmonic force. . . . .	16
4.6	Model of a forced damped spring-mass-system, where the spring foot point is excited by a harmonic displacement. . . . .	17
4.7	Model of a forced damped spring-mass system, where the damper foot point is excited by a harmonic displacement. . . . .	18
4.8	Model of a forced damped spring-mass-system where the spring as well as the damper foot point are excited with a sinusoidal displacement. . . . .	19
4.9	Transfer functions of a damped spring-mass-system, where the damper footpoint and the damper and spring footpoints are excited . . . . .	20
5.1	Basic design of a vibration sensor. . . . .	22
5.2	Spring element layout with equivalent string system . . . . .	23
5.3	Single plate capacitor. . . . .	24
5.4	Differential capacitor . . . . .	25
5.5	A detailed representation of the freestanding mass sensor design. . . . .	25
6.1	Cross section of silicon nitride coated wafer. . . . .	27

6.2	Metal layer deposition on a conventional resist . . . . .	30
6.3	Production steps for metal layer deposition using image reversible resist . .	31
6.4	Backside cavity etch process . . . . .	33
7.1	Image of the Micro System Analyser (MSA). . . . .	35
7.2	Working principle of the laser interferometry mode, utilizing the Doppler effect. . . . .	36
7.3	Example of an exposure cycle for measuring in-plane displacement using a series of LED flashes. . . . .	38
7.4	Example of two consecutive exposures of an arbitrary vibrating specimen. .	39
7.5	Simplified model of the topographical measurement mode of the MSA using a Mirau objective. . . . .	40
8.1	Basic set-up of shaker. . . . .	46
8.2	Forces applied on chip holder and Si-chip. . . . .	49
8.3	Equivalent circuit of the piezoelectric stack. . . . .	51
8.4	Assembly of the shaker for Si based accelerator sensors. . . . .	53
8.5	Harmonic displacement of the holder at 5 kHz and $\hat{u} = 7.8$ V. . . . .	54
8.6	Shaker mounted for out-of-plane measurement. . . . .	55
8.7	Displacement of holder at 7.8 V . . . . .	56
8.8	Enhanced spring–mass–system model of shaker. . . . .	57
8.9	Displacement of holder and PEEK frame at 3.9 V. . . . .	58
8.10	Displacement of holder at 15 kHz. . . . .	60
8.11	Displacement and drive current of shaker. . . . .	61
8.12	Frequency characteristics of shaker at 1 and 7.8 V. . . . .	62
8.13	Displacement of shaker at 9.2 and 8.9 kHz. . . . .	63
8.14	Displacement of shaker at 10 kHz. . . . .	64

10.1	Microscopic overview of a vibration sensor. . . . .	67
10.2	Micrograph of the top side of a test sensor. . . . .	68
10.3	Micrograph of the backside of a test sensor. . . . .	68
10.4	Micrograph of the top side of a test sensor. . . . .	69
10.5	Microscopic picture of the backside of a test sensor. . . . .	69
10.6	Micrograph that depicts stiction between spring beams. . . . .	69
10.7	Micrograph of correctly separated spring beams. . . . .	69
10.8	Micrograph of a vibration sensor were the seismic mass is dislocated under the frame of the sensor. . . . .	70
10.9	Frequency response of a vibration sensor. . . . .	71
10.10	Frequency response around a resonance peak with a resolution of 5 Hz. . .	72
10.11	Maximum positive $x$ -axis displacement at 3.15 kHz. . . . .	73
10.12	Maximum negative $x$ -axis displacement at 3.15 kHz. . . . .	73
10.13	Maximum displacement in positive $y$ -direction. . . . .	73
10.14	Maximum displacement in negative $y$ -direction. . . . .	73
10.15	Micrograph of one of the springs of a test sensor. . . . .	74